

See discussions, stats, and author profiles for this publication at: <https://www.researchgate.net/publication/321141768>

Influence of coupled fields on free vibration and static behavior of functionally graded magneto-electro-thermo-elastic plate

Article in *Journal of Intelligent Material Systems and Structures* · November 2017

DOI: 10.1177/1045389X17740739

CITATIONS

24

READS

237

3 authors, including:



Vinyas Mahesh

Indian Institute of Science

82 PUBLICATIONS 572 CITATIONS

[SEE PROFILE](#)



Subhaschandra Kattimani

National Institute of Technology Karnataka

32 PUBLICATIONS 533 CITATIONS

[SEE PROFILE](#)

Some of the authors of this publication are also working on these related projects:



Hard Thin Films performance and characteristics [View project](#)



Experimental characterisation and numerical modelling of delamination growth in Fiber Reinforced Polymer laminated composites under cyclic loading [View project](#)

Influence of coupled fields on free vibration and static behavior of functionally graded magneto-electro-thermo-elastic plate

Journal of Intelligent Material Systems
and Structures

1–26

© The Author(s) 2017

Reprints and permissions:

sagepub.co.uk/journalsPermissions.nav

DOI: 10.1177/1045389X17740739

journals.sagepub.com/home/jim



Vinyas Mahesh, Piyush J Sagar and Subhaschandra Kattimani

Abstract

In this article, the influence of full coupling between thermal, elastic, magnetic, and electric fields on the natural frequency of functionally graded magneto-electro-thermo-elastic plates has been investigated using finite element methods. The contribution of overall coupling effect as well as individual elastic, piezoelectric, piezomagnetic, and thermal phases toward the stiffness of magneto-electro-thermo-elastic plates is evaluated. A finite element formulation is derived using Hamilton's principle and coupled constitutive equations of magneto-electro-thermo-elastic material. Based on the first-order shear deformation theory, kinematics relations are established and the corresponding finite element model is developed. Furthermore, the static studies of magneto-electro-elastic plate have been carried out by reducing the fully coupled finite element formulation to partially coupled state. Particular attention has been paid to investigate the influence of thermal fields, electric fields, and magnetic fields on the behavior of magneto-electro-elastic plate. In addition, the effect of pyrocoupling on the magneto-electro-elastic plate has also been studied. Furthermore, the effect of geometrical parameters such as aspect ratio, length-to-thickness ratio, stacking sequence, and boundary conditions is studied in detail. The investigation may contribute significantly in enhancing the performance and applicability of functionally graded magneto-electro-thermo-elastic structures in the field of sensors and actuators.

Keywords

Magneto-electro-elastic, coupled fields, functionally graded, magneto-thermo-electro-elastic, pyroeffect

Introduction

A great deal of attention has been paid to develop composite structures which can respond in more adaptive and controlled way to the external stimuli. Such adaptive structures exhibit better versatility and ability to respond in a controlled manner. This results in minimizing the overall size of the structure. To obtain such properties, it is necessary to combine two or more smart materials. The combination of piezoelectric (PE) and magnetostrictive materials has gained the attention of the researchers due to their highest coupling properties. This unique class of smart composite made of PE and magnetostrictive materials also provides a wide range of applicability by virtue of its product properties, such as electro-elastic, magneto-elastic, and electromagnetic coupling, and they are commonly termed as magneto-electro-elastic (MEE) composites. These composites possess a special property of converting energy among electric, magnetic, and mechanical energy. To utilize these coupling properties effectively,

it is important to unearth the structural behavior of these smart laminated MEE composites in the presence of thermal, electric, and magnetic field environment. Furthermore, the MEE structures with functionally graded material in the thermal environment have been a recent trend, as it exhibits an additional pyroelectric and pyromagnetic coupling. Due to these advanced properties, functionally graded magneto-electro-thermo-elastic (FG-METE) structures have seen its potential applications in the field of aeronautics, nano-electronics, non-volatile memories, robotics, medical, and sonar applications.

Department of Mechanical Engineering, National Institute of Technology
Karnataka, Surathkal, India

Corresponding author:

Subhaschandra Kattimani, Department of Mechanical Engineering,
National Institute of Technology Karnataka, Surathkal 575025, India.
Email: sck@nitk.ac.in; subhaskatti@gmail.com

Many pioneers have contributed toward various analyses of MEE structures such as free vibration analysis, static analysis, and buckling analysis. Moita et al. (2009) investigated the static and vibration behavior of the MEE plate subjected to mechanical loading using higher-order shear deformation plate theory. Sladek et al. (2013) developed a mesh-less method to examine the dynamic problems of thick MEE plates. Annigeri et al. (2007) carried out free vibration analysis of multilayered MEE beam using in-plane finite element (FE) analysis. Ramirez et al. (2006) developed an approximate solution of two-dimensional MEE laminates for the free vibration analysis, in which discrete layer approach along with the Ritz method was implemented. Bhangale and Ganesan (2006) adopted a semi-analytical FE procedure to investigate the free vibration characteristics of the functionally graded MEE plates. Shooshtari and Razavi (2015a, 2015b) and Razavi and Shooshtari (2015) developed an analytical formulation for nonlinear free vibration analysis of symmetrically laminated MEE plate and doubly curved shell resting on an elastic foundation. Pan (2001) and Pan and Heyliger (2002) studied exact solutions and free vibrations for anisotropic MEE plates under static loadings using the propagator matrix to obtain the solutions for multilayered plates. Xin and Hu (2015) developed semi-analytical solutions for free vibration of MEE plates using hybrid analysis. Chen et al. (2007) used state vector approach to analyze the free vibration of MEE laminate plates. Huang et al. (2007) analyzed the plane stress problem of anisotropic FG MEE beams and formulated the analytical solutions. Xin and Hu (2015) used three-dimensional (3D) elasticity theory for deriving semi-analytical solutions of MEE beams for free vibration with the application of the state-space approach (SSA) and discrete singular convolution (DSC) algorithm. Kattimani and Ray (2014a, 2014b) investigated the active control of geometrically nonlinear vibrations of MEE plates and doubly curved shells. They extended their analysis to the FG MEE plates also (Kattimani and Ray, 2015). The smart structures should be designed accurately for the application of sensors and actuators. Thus, it is very much important to determine the variations of static parameters under the influence of various loads. Lage et al. (2004, 2005) have derived a partial mixed layer-wise FE formulation to study the static and free behavior of MEE plates. Daga et al. (2009) presented the FE modeling for investigating the transient behavior of MEE materials subjected to different mechanical load and boundary conditions. Wang et al. (2003) derived the state vector equations for 3D, orthotropic and linearly MEE media using governing equations. Phoenix et al. (2009) performed the static and dynamic analysis of coupled MEE plates using the Reissner mixed variational theorem. Also, few literature addressing the effects of coupling factors on the structural behavior of

MEE multilayered structures using equivalent single layer and layer-wise models have proved to be handy (Alaimo et al., 2013; Benedetti and Milazzo, 2017; Milazzo, 2013, 2014a, 2014b).

A significant change in response of the structure is observed when MEE structures are subjected to thermal, electric, and/or magnetic field. Under thermal loading, MEE structures experiences coupled thermo-elastic, pyroelectric, and pyromagnetic effects which can bring drastic variation in the structural response of MEE structures. Tan and Tong (2002) presented two micromechanics model for investigating the electrothermo-magneto-elastic properties of the PE-piezomagnetic (PM) composite. They also studied the effect of volume fraction (V_f). Kondaiah et al. (2012, 2013) studied the static behavior of 3D MEE beams and plates subjected to uniform temperature loads considering the effects of pyroelectric and pyromagnetic properties. The influence of different volume fractions of $\text{BaTiO}_3\text{-CoFe}_2\text{O}_4$ is also investigated. Kumaravel et al. (2007, 2010) used the FE model for linear buckling and vibration behavior of multiphase MEE cantilever beam and studied the influence of material constants on critical buckling load. Vinyas and Kattimani (2017a, 2017b, 2017c) analyzed the static behavior of MEE structures (plates and beams) under the influence of different thermal loads. Recently, they extended their investigation for evaluating the hygrothermal response of MEE plates (Vinyas and Kattimani, 2017d).

Gao et al. (2010) analyzed the behavior of MEE plate by formulating an analytical solution in a transient magnetic field. Lee and Lin (2010) developed a transverse magnetic force model for the interface between the air and ferromagnetic material along with the continuation of magneto-elastic stress throughout the material boundary. Wei et al. (2007) analyzed magnetic traction on a deformable ferromagnetic material and studied the vibration frequency of a ferromagnetic beam subjected to an inclined magnetic field. Wang et al. (2011) studied the transient response of MEE composite plate using 3D FE modeling with the aid of commercial software. Vaezi et al. (2016) carried out frequency analysis and buckling of an MEE composite beam using Euler-Bernoulli beam theory when external magnetic and electric potentials were applied over the beam. Ebrahimi and Barati (2016a, 2016b) and Ebrahimi and Salari (2015) studied the thermal vibration behavior of FG-METE nanobeams based on a higher-order shear deformation beam theory. They also investigated the effects of thermal loadings, magnetic potential, external electric voltage, power-law index, nonlocal parameter, and slenderness ratio on the vibration response. It is evident from the literature that few investigations are reported on fully coupled constitutive relations of thermal, electric, and elastic fields. Among them, Oh and Cho (2004) developed a three-noded triangular FE based on cubic zigzag plate theory to

predict fully coupled behavior of thermo-electro-elastic fields. Ahmad et al. (2006) derived a coupled electro-thermo-elastic equations from the fundamental principles of mass, linear momentum, angular momentum, energy, and charge conservation. Pérez-Fernández et al. (2009) presented different types of constitutive relations of thermo-magneto-electro-elasticity using solid thermodynamics. Soh and Liu (2005) discussed the mathematical properties of the thermodynamic potentials and the relations between the material constants. Furthermore, they also derived various forms of the constitutive equations of MEE solids with the thermodynamic potential corresponding to each form.

From the extensive literature survey, it is found that abundant research is reported on the free vibration and static analysis of MEE plate. To the best of authors' knowledge, no work has been reported on analyzing the influence of various coupled and individual phases on the natural frequency of MEE plates by considering full coupling of thermal fields with elastic, magnetic, and electric fields. Furthermore, the static analysis of FG-METE-laminated composite plate subjected to different field forces, namely, thermal, electric, and magnetic, are not found in the literature. Consequently, this study is devoted to understand the static and free vibration behavior of FG-METE plates. The FE model has been developed by incorporating first-order shear deformation theory (FSDT). The governing equation of motion is derived using Hamilton's principle and fully coupled constitutive equations. This study also attempts to evaluate the influence of pyroeffects, boundary conditions, aspect ratio, stacking sequence, and length-to-thickness ratio on the free and static behavior of FG-METE plates.

Problem description and governing equations

Plate geometry and displacement relation

A schematic representation of METE plate with constant thickness H made of N layers shown in Figure 1 is considered for the analysis. Each layer is made of different volume fractions (V_f) of barium titanate (BaTiO_3) and cobalt ferric oxide (CoFe_2O_4), as shown in Figure 2. The length a , breadth b , and thickness H adjoins the x , y , and z axes of Cartesian co-ordinates. The in-plane displacements u , v , and w are assumed to follow the FSDT, which can be written as follows

$$\begin{aligned} u &= u_0 + z\theta_x \\ v &= v_0 + z\theta_y \\ w &= w_0 \end{aligned} \quad (1)$$

in which u_0 , v_0 , and w_0 are the midplane displacements along x , y , and z axes, respectively. θ_x and θ_y are the

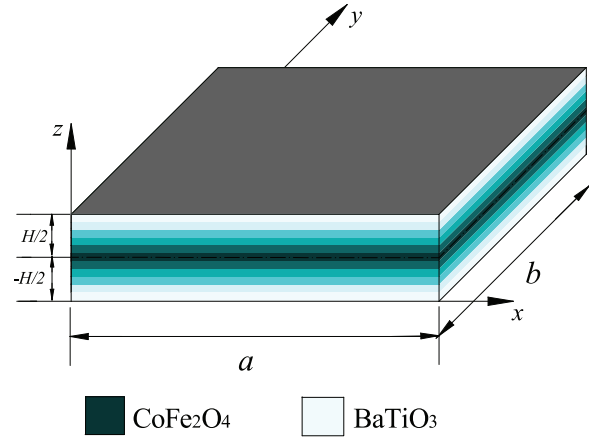


Figure 1. Schematic diagram of MEE plate.

rotations of the portions of the normal lying in the xz plane and yz plane, respectively. The reference plane ($z = 0$) is chosen at the midplane of the laminate.

Layer-wise FG-METE plates

A layer-wise FG-METE plates are modeled by considering two forms of ply arrangement, namely, *FG-PMP* and *FG-MPM* METE plates. The term *P* corresponds to pure PE phase and *M* corresponds to pure PM phase. For *FG-PMP* stacking sequence, the top layer has pure PE composition which reduces in finite steps of $0.2 V_f$ across the thickness and plummets to pure PM phase at the mid-layer of the plate ($z = 0$), as shown in Figure 2(a). This again raises to pure PE phase at the bottommost layer of the plate. For *FG-MPM* stacking sequence, the sequential arrangement is vice versa, as represented in Figure 2(b).

Constitutive equations

In this study, it is assumed that the electric, magnetic, thermal, and elastic fields of an anisotropic METE solid are fully and linearly coupled. The corresponding constitutive equations can be written as follows

$$\begin{aligned} \{\sigma\} &= [C]\{\varepsilon\} - [e]\{E\} - [q]\{H\} - [\lambda]\{\theta\} \\ \{D\} &= [e]^T\{\varepsilon\} + [d]\{E\} + [m]\{H\} + [p_e]\{\theta\} \\ \{B\} &= [q]^T\{\varepsilon\} + [m]^T\{E\} + [\mu]\{H\} + [p_m]\{\theta\} \\ \{\eta\} &= [\lambda]^T\{\varepsilon\} + [p_e]^T\{E\} + [p_m]^T\{H\} + a\{\theta\} \end{aligned} \quad (2)$$

where $\{\sigma\}$, $\{D\}$, $\{B\}$, and $\{\eta\}$ represent the stress vector, electric displacement vector, magnetic induction vector, and entropy, respectively. $\{\varepsilon\}$, $\{E\}$, $\{H\}$, and $\{\theta\}$ are strain vector, electric field vector, magnetic field vector, and temperature rise, respectively. $[C]$, $[d]$, and $[\mu]$ are the elastic, PE, and magnetostrictive coefficient matrices, respectively. Furthermore, a is the heat

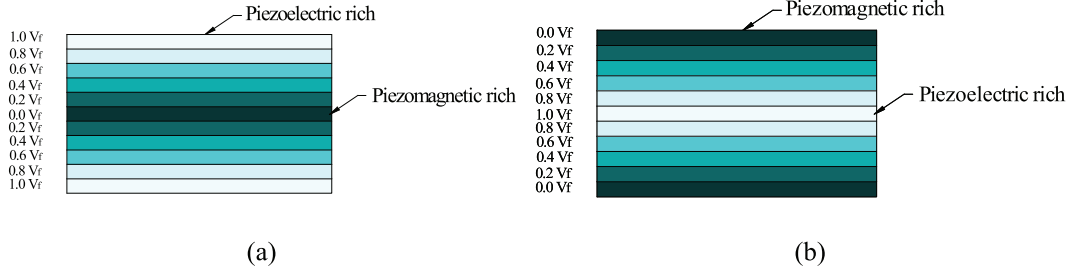


Figure 2. Schematic diagram of functionally graded plate showing (a) FG-P/M/P stacking sequence and (b) FG-M/P/M stacking sequence.

capacity per unit volume given by $a = \rho C_E / T_0$, where C_E is the specific heat of the material. $[e]$, $[q]$, $[\lambda]$, $[m]$, $[p_e]$, and $[p_m]$ are PE, PM, thermal stress moduli, electromagnetic, pyroelectric, and pyromagnetic material coefficient, respectively. These constitutive equations can be described in more generalized global matrix form as follows

$$\begin{aligned} \{d_t\} &= [N_t]\{d_t^e\}; \{d_r\} = [N_r]\{d_r^e\}; \\ \{\phi\} &= [N_\phi]\{\phi^e\}; \{\psi\} = [N_\psi]\{\psi^e\}; \{\theta\} = [N_\theta]\{\theta^e\} \end{aligned} \quad (5)$$

in which

$$\begin{Bmatrix} \sigma_1 \\ \sigma_2 \\ \sigma_3 \\ \sigma_{23} \\ \sigma_{13} \\ \sigma_{12} \\ D_x \\ D_y \\ D_z \\ B_x \\ B_y \\ B_z \\ \eta \end{Bmatrix} = \begin{bmatrix} c11 & c12 & c13 & 0 & 0 & 0 & 0 & 0 & e31 & 0 & 0 & q31 & \lambda1 \\ c12 & c22 & c23 & 0 & 0 & 0 & 0 & 0 & e31 & 0 & 0 & q31 & \lambda2 \\ c13 & c23 & c33 & 0 & 0 & 0 & 0 & 0 & e33 & 0 & 0 & q33 & \lambda3 \\ 0 & 0 & 0 & c44 & c45 & 0 & 0 & e15 & 0 & 0 & q15 & 0 & 0 \\ 0 & 0 & 0 & c45 & c55 & 0 & e15 & 0 & 0 & q15 & 0 & 0 & 0 \\ 0 & 0 & 0 & 0 & 0 & c66 & 0 & 0 & 0 & 0 & 0 & 0 & 0 \\ 0 & 0 & 0 & 0 & e15 & 0 & d11 & 0 & 0 & m11 & 0 & 0 & 0 \\ 0 & 0 & 0 & e15 & 0 & 0 & 0 & d22 & 0 & 0 & m22 & 0 & p_e \\ e31 & e31 & e33 & 0 & 0 & 0 & 0 & 0 & d33 & 0 & 0 & m33 & 0 \\ 0 & 0 & 0 & 0 & q15 & 0 & m11 & 0 & 0 & \mu11 & 0 & 0 & 0 \\ 0 & 0 & 0 & q15 & 0 & 0 & 0 & m22 & 0 & 0 & \mu22 & 0 & p_m \\ q31 & q31 & q33 & 0 & 0 & 0 & 0 & 0 & m33 & 0 & 0 & \mu33 & 0 \\ \lambda1 & \lambda2 & \lambda3 & 0 & 0 & 0 & 0 & p_e & 0 & 0 & p_m & 0 & a \end{bmatrix} * \begin{Bmatrix} \varepsilon_x \\ \varepsilon_y \\ \varepsilon_z \\ \gamma_{xz} \\ \gamma_{yz} \\ \gamma_{xy} \\ E_x \\ E_y \\ E_z \\ H_x \\ H_y \\ H_z \\ \theta \end{Bmatrix} \quad (3)$$

FE formulation

The METE plate is discretized into eight-noded quadrilateral element with each node having eight degrees of freedom, namely, three translational (u , v , and w), two rotational (θ_x and θ_y), and one for each electric potential (ϕ), magnetic potential (ψ), and temperature rise (θ). The generalized translational displacement vector and rotational vector associated with the i th ($i = 1, 2, 3, \dots, 8$) node of the element can be represented as follows

$$\{d_{ii}\} = [u_i v_i w_i]^T, \{d_{ri}\} = [\theta_x \theta_y]^T \quad (4)$$

The generalized translational vector $\{d_t\}$, rotational vector $\{d_r\}$, electric potential vector $\{\phi\}$, magnetic potential vector $\{\psi\}$, and temperature $\{\theta\}$ at any point within the element can be represented in terms of the nodal displacement vector, nodal electric potential, nodal magnetic potential vector, and nodal temperature rise, respectively, as follows

$$\begin{aligned} \{d_t^e\} &= [\{d_{t1}\}^T \{d_{t2}\}^T \dots \{d_{t8}\}^T]^T, \\ \{d_r^e\} &= [\{d_{r1}\}^T \{d_{r2}\}^T \dots \{d_{r8}\}^T]^T \\ \{\phi^e\} &= [\phi_1 \phi_2 \dots \phi_8]^T, \{\psi^e\} = [\psi_1 \psi_2 \dots \psi_8]^T, \\ \{\theta^e\} &= [\theta_1 \theta_2 \dots \theta_8]^T \\ [N_t] &= [N_{t1} N_{t2} \dots N_{t8}], N_{ti} = N_i I_t, \\ [N_r] &= [N_{r1} N_{r2} \dots N_{r8}], N_{ri} = N_i I_r \\ [N_\psi] &= [N_\theta] = [N_\phi] = [N_1 N_2 \dots N_8] \end{aligned} \quad (6)$$

where N_i is the natural co-ordinate shape function associated with the i th node of the quadrilateral element. I_t and I_r are (3×3) and (2×2) identity matrices, respectively. Using the FSDT for plates, strains can be related to the nodal degree of freedom as follows

$$\begin{aligned} \{\varepsilon_b\} &= [B_{tb}]\{d_t^e\} + z[B_{rb}]\{d_r^e\} \\ \{\varepsilon_s\} &= [B_{ts}]\{d_t^e\} + [B_{rs}]\{d_r^e\} \end{aligned} \quad (7)$$

where the derivative of shape function matrices $[B_{ib}]$, $[B_{rb}]$, $[B_{ts}]$, and $[B_{rs}]$ can be expressed as follows

$$\begin{aligned} [B_{ib}] &= \begin{bmatrix} \frac{\partial Ni}{\partial x} & 0 & 0 \\ 0 & \frac{\partial Ni}{\partial y} & 0 \\ \frac{\partial Ni}{\partial y} & \frac{\partial Ni}{\partial x} & 0 \end{bmatrix}, [B_{rb}] = \begin{bmatrix} \frac{\partial Ni}{\partial x} & 0 \\ 0 & \frac{\partial Ni}{\partial y} \\ \frac{\partial Ni}{\partial y} & \frac{\partial Ni}{\partial x} \end{bmatrix}, \\ [B_{ts}] &= \begin{bmatrix} 0 & 0 & \frac{\partial Ni}{\partial x} \\ 0 & 0 & \frac{\partial Ni}{\partial y} \end{bmatrix}, [B_{rs}] = \begin{bmatrix} 1 & 0 \\ 0 & 0 \end{bmatrix} \end{aligned} \quad (8)$$

in which the derivative of shape function matrices $[B_\phi]$ and $[B_\psi]$ can be expressed as follows

$$[B_{\phi i}] = [B_{\psi i}] = \begin{bmatrix} \frac{\partial Ni}{\partial x} & \frac{\partial Ni}{\partial y} & \frac{\partial Ni}{\partial z} \end{bmatrix}^T \quad (11)$$

Evaluation of elemental equation of motion

The governing equation of motion for FG-METE plate with N layers is derived by considering the first variations of total potential energy T_p and kinetic energy T_k and employing Hamilton's principle as follows

$$\begin{aligned} \delta T_p &= \frac{1}{2} \sum_{k=1}^N \int_{\Omega^k} \delta \{\varepsilon_b\}^T \{\sigma_b\} d\Omega^k - \frac{1}{2} \sum_{k=1}^N \int_{\Omega^k} \delta \{\varepsilon_s\}^T \{\sigma_s\} d\Omega^k - \frac{1}{2} \sum_{k=1}^N \int_{\Omega^k} \delta \{E\}^T \{D\} d\Omega^k - \frac{1}{2} \sum_{k=1}^N \int_{\Omega^k} \delta \{H\}^T \{B\} d\Omega^k \\ &\quad - \frac{1}{2} \sum_{k=1}^N \int_{\Omega^k} \delta \{\theta\}^T \{\eta\} d\Omega^k - \int_A \delta \{d_t\}^T \{f\} dA - \int_A \delta \{\phi\} Q^\phi dA - \int_A \delta \{\psi\} Q^\psi dA - \int_A \delta \{\theta\} \bar{q} dA \end{aligned} \quad (12a)$$

The electric field and the magnetic field vectors are a negative gradient of electric and magnetic potentials, respectively. Using derivative of shape function matrices, the electric field, and the magnetic field can be related to the nodal electric potential and nodal magnetic potential, respectively, as follows

$$\begin{aligned} \{E\} &= \{E_x, E_y, E_z\} = \left\{ -\frac{\partial \phi}{\partial x}, -\frac{\partial \phi}{\partial y}, -\frac{\partial \phi}{\partial z} \right\} \\ &= -[B_\phi] \{\phi^e\} \end{aligned} \quad (9)$$

$$\begin{aligned} \{H\} &= \{H_x, H_y, H_z\} = \left\{ -\frac{\partial \psi}{\partial x}, -\frac{\partial \psi}{\partial y}, -\frac{\partial \psi}{\partial z} \right\} \\ &= -[B_\psi] \{\psi^e\} \end{aligned} \quad (10)$$

$$\delta T_k = \int_{\Omega^k} \delta \{d_t\}^T \rho \{\ddot{d}_t\} d\Omega^k \quad (12b)$$

where k denotes the layer number. $\{f\}$, Q^ϕ , Q^ψ , and \bar{q} are the mechanical field force, electric surface charge density, magnetic flux density, and heat flux, respectively, acting over an area A . The volume of the k th layer is represented by Ω^k . Since the METE plate thickness considered for the analysis is very thin, the rotary inertia may be neglected (Panda and Ray, 2008, 2009; Ray and Shivakumar, 2009). Substituting the constitutive equations (equation (2) into equation (12)), the equilibrium equations of motions can be obtained as follows

$$\begin{aligned} &\frac{1}{2} \sum_{k=1}^N \delta \left(\int_{\Omega^k} \{\varepsilon_b\}^T [C_b^k] \{\varepsilon_b\} d\Omega^k - \int_{\Omega^k} \{\varepsilon_b\}^T [e^k] \{E\} d\Omega^k - \int_{\Omega^k} \{\varepsilon_b\}^T [q^k] \{H\} d\Omega^k - \int_{\Omega^k} \{\varepsilon_b\}^T [\lambda^k] \{\theta\} d\Omega^k \right) \\ &\quad - \frac{1}{2} \sum_{k=1}^N \delta \left(\int_{\Omega^k} \{\varepsilon_s\}^T [C_s^k] \{\varepsilon_s\} d\Omega^k \right) \\ &\quad - \frac{1}{2} \sum_{k=1}^N \delta \left(\int_{\Omega^k} \{E\}^T [e^k]^T \{\varepsilon_b\} d\Omega^k - \int_{\Omega^k} \{E\}^T [n^k] \{E\} d\Omega^k - \int_{\Omega^k} \{E\}^T [m^k] \{H\} d\Omega^k - \int_{\Omega^k} \{E\}^T [p_e^k] \{\theta\} d\Omega^k \right) \\ &\quad - \frac{1}{2} \sum_{k=1}^N \delta \left(\int_{\Omega^k} \{H\}^T [q^k]^T \{\varepsilon_b\} d\Omega^k - \int_{\Omega^k} \{H\}^T [m^k] \{E\} d\Omega^k - \int_{\Omega^k} \{H\}^T [\mu^k] \{H\} d\Omega^k - \int_{\Omega^k} \{H\}^T [p_m^k] \{\theta\} d\Omega^k \right) \\ &\quad - \frac{1}{2} \sum_{k=1}^N \delta \left(\int_{\Omega^k} \{\theta\}^T [\lambda^k]^T \{\varepsilon_b\} d\Omega^k - \int_{\Omega^k} \{\theta\}^T [p_e^k] \{E\} d\Omega^k - \int_{\Omega^k} \{\theta\}^T [p_m^k] \{H\} d\Omega^k - \int_{\Omega^k} \{\theta\}^T [a] \{\theta\} d\Omega^k \right) \\ &\quad - \int_A \delta \{d_t\}^T \{f\} dA - \int_A \delta \{\phi\} Q^\phi dA - \int_A \delta \{\psi\} Q^\psi dA - \int_A \delta \{\theta\} \bar{q} dA + \int_{\Omega^k} \delta \{d_t\}^T \rho \{\ddot{d}_t\} d\Omega^k \end{aligned} \quad (13)$$

Substituting equations (5) to (11) in equation (13), we obtain the following

$$\begin{aligned}
& \frac{1}{2} \sum_{k=1}^N \int_{\Omega^k} \delta([B_{tb}]\{d_t^e\} + z[B_{rb}]\{d_r^e\})^T [C_b^k] ([B_{tb}]\{d_t^e\} + z[B_{rb}]\{d_r^e\}) d\Omega^k \\
& - \frac{1}{2} \sum_{k=1}^N \int_{\Omega^k} \delta([B_{tb}]\{d_t^e\} + z[B_{rb}]\{d_r^e\})^T [e^k] [B_\phi] \{\phi\}^e d\Omega^k \\
& - \frac{1}{2} \sum_{k=1}^N \int_{\Omega^k} \delta([B_{tb}]\{d_t^e\} + z[B_{rb}]\{d_r^e\})^T [q^k] [B_\psi] \{\psi\}^e d\Omega^k \\
& - \frac{1}{2} \sum_{k=1}^N \int_{\Omega^k} \delta([B_{tb}]\{d_t^e\} + z[B_{rb}]\{d_r^e\})^T [\lambda^k] [N_\phi] \{\theta\}^e d\Omega^k \\
& - \frac{1}{2} \sum_{k=1}^N \int_{\Omega^k} \delta([B_{ts}]\{d_t^e\} + [B_{rs}]\{d_r^e\})^T [C_s^k] ([B_{ts}]\{d_t^e\} + [B_{rs}]\{d_r^e\}) d\Omega^k \\
& - \frac{1}{2} \sum_{k=1}^N \int_{\Omega^k} \delta([B_\phi] \{\phi^e\})^T \left\{ [e^k]^T [B_{tb}]\{d_t^e\} + [e^k]^T [B_{rb}]\{d_r^e\} + [d^k] [B_\phi] \{\phi^e\} + [m^k] [B_\psi] \{\psi^e\} + [p_e^k] [N_\theta] \{\theta^e\} \right\} d\Omega^k \\
& - \frac{1}{2} \sum_{k=1}^N \int_{\Omega^k} \delta([B_\psi] \{\psi^e\})^T \left\{ [q^k]^T [B_{tb}]\{d_t^e\} + [q^k]^T z[B_{rb}]\{d_r^e\} + [m^k] [B_\phi] \{\phi^e\} + [\mu^k] [B_\psi] \{\psi^e\} + [p_m^k] [N_\theta] \{\theta^e\} \right\} d\Omega^k \\
& - \frac{1}{2} \sum_{k=1}^N \int_{\Omega^k} \delta([N_\theta] \{\theta^e\})^T \left\{ [C_b^k] \{\alpha^k\} [B_{tb}]\{d_t^e\} + [C_b^k] \{\alpha^k\} z[B_{rb}]\{d_r^e\} + [p_e^k]^T [B_\phi] \{\phi^e\} + [p_m^k]^T [B_\psi] \{\psi^e\} + a[N_\theta] \{\theta^e\} \right\} d\Omega^k \\
& - \int_A \{d_t^e\}^T \{F_m^e\} - \int_A \delta\{\phi^e\}^T \{F_\phi^e\} - \int_A \delta\{\psi^e\}^T \{F_\psi^e\} - \int_A \delta\{\theta^e\}^T \{F_q^e\} + [M_{tt}^e] \{\ddot{d}_t^e\}
\end{aligned} \tag{14}$$

The simplification of these equations will lead to equations of motions for the fully coupled FG-METE plate

$$\begin{aligned}
& [M_{tt}^e] \{\ddot{d}_t^e\} + [K_{tt}^e] \{d_t^e\} + [K_{tr}^e] \{d_r^e\} \\
& + [K_{t\phi}^e] \{\phi^e\} + [K_{t\psi}^e] \{\psi^e\} + [K_{t\theta}^e] \{\theta^e\} = \{F_{t-m}^e\} \\
& [K_{tr}^e]^T \{d_t^e\} + [K_{rr}^e] \{d_r^e\} + [K_{r\phi}^e] \{\phi^e\} \\
& + [K_{r\psi}^e] \{\psi^e\} + [K_{r\theta}^e] \{\theta^e\} = \{F_{r-m}^e\} \\
& [K_{t\phi}^e]^T \{d_t^e\} + [K_{r\phi}^e]^T \{d_r^e\} - [K_{\phi\phi}^e] \{\phi^e\} \\
& - [K_{\phi\psi}^e] \{\psi^e\} - [K_{\phi\theta}^e] \{\theta^e\} = \{F_\phi^e\} \\
& [K_{t\psi}^e]^T \{d_t^e\} + [K_{r\psi}^e]^T \{d_r^e\} - [K_{\psi\psi}^e] \{\psi^e\} \\
& - [K_{\psi\phi}^e] \{\phi^e\} - [K_{\psi\theta}^e] \{\theta^e\} = \{F_\psi^e\} \\
& [K_{t\theta}^e]^T \{d_t^e\} + [K_{r\theta}^e]^T \{d_r^e\} - [K_{\theta\theta}^e] \{\theta^e\} \\
& - [K_{\theta\psi}^e] \{\psi^e\} - [K_{\theta\phi}^e] \{\phi^e\} = \{F_q^e\}
\end{aligned} \tag{15}$$

where $[M_{tt}^e]$ is the mass matrix; $[K_{tt}^e]$, $[K_{tr}^e]$, and $[K_{rr}^e]$ are elastic stiffness matrices; $[K_{t\phi}^e]$ and $[K_{r\phi}^e]$ are coupled electro-elastic stiffness matrices; $[K_{t\psi}^e]$ and $[K_{r\psi}^e]$ are coupled magneto-elastic stiffness matrices; $[K_{t\theta}^e]$ and $[K_{r\theta}^e]$ are coupled thermo-elastic stiffness matrices; $[K_{\phi\phi}^e]$, $[K_{\psi\psi}^e]$, and $[K_{\theta\theta}^e]$ are electrical, magnetic, and thermal stiffness matrices, respectively; $[K_{\phi\psi}^e]$ and $[K_{\psi\phi}^e]$ are coupled pyroelectric and pyromagnetic stiffness matrices, respectively; and $[K_{\phi\psi}^e]$ is coupled electromagnetic stiffness matrix; $\{F_{t-m}^e\}$ and $\{F_{r-m}^e\}$ are the

mechanical force vectors; $\{F_\phi^e\}$, $\{F_\psi^e\}$, and $\{F_q^e\}$ are the electrical force vector, magnetic force vector, and temperature force vectors, respectively. In order to analyze the overall FG-METE plate, local-global transformation is carried out for each elemental matrix and equivalent global mass matrix $[M_{tt}]$, stiffness matrix $[K_{eq}]$, and force matrix $\{F_{eq}\}$ are obtained. Thus, the obtained equations are globalized and the equilibrium equations are condensed (Appendix 1) to represent in a simple form as follows

$$[M_{tt}] \{\ddot{d}_t\} + [K_{eq}] \{d_t\} = \{F_{eq}\} \tag{16}$$

For free vibration analysis, equation (16) reduces to the following form

$$[M_{tt}] \{\ddot{d}_t\} + [K_{eq}] \{d_t\} = 0 \tag{17}$$

Equation (17) can be represented in the matrix form as follows

$$\left(\begin{bmatrix} K_{tt} & K_{tr} & K_{t\phi} & K_{t\psi} & K_{t\theta} \\ K_{rt} & K_{rr} & K_{r\phi} & K_{r\psi} & K_{r\theta} \\ K_{\phi t} & K_{\phi r} & K_{\phi\phi} & K_{\phi\psi} & K_{\phi\theta} \\ K_{\psi t} & K_{\psi r} & K_{\psi\phi} & K_{\psi\psi} & K_{\psi\theta} \\ K_{\theta t} & K_{\theta r} & K_{\theta\phi} & K_{\theta\psi} & K_{\theta\theta} \end{bmatrix} - \omega^2 \begin{bmatrix} M_{tt} & 0 & 0 & 0 & 0 \\ 0 & 0 & 0 & 0 & 0 \\ 0 & 0 & 0 & 0 & 0 \\ 0 & 0 & 0 & 0 & 0 \\ 0 & 0 & 0 & 0 & 0 \end{bmatrix} \right) \begin{Bmatrix} d_t \\ d_r \\ \phi \\ \psi \\ \theta \end{Bmatrix} = \begin{Bmatrix} 0 \\ 0 \\ 0 \\ 0 \\ 0 \end{Bmatrix}$$

(18)

where $[M_{ii}]$, $[K_{eq}]$, and $\{F_{eq}\}$ are global mass matrix, global equivalent stiffness matrix, and global equivalent force vector, respectively.

Furthermore, for the static analysis, the fully coupled equilibrium equations for FG-METE are reduced with the help of the following assumptions:

1. Thermal fields are partially coupled with magneto-electro-elastic fields. Hence, the thermal effects can be treated as external loads.
2. The effect of externally applied electric charge and magnetic current is not zero.

Considering the above assumptions, the equations of motion for METE plates in the static case accounting for different loading conditions can be rewritten as follows

$$\begin{aligned}
& [K_{ii}^e] \{d_i^e\} + [K_{ir}^e] \{d_r^e\} + [K_{i\phi}^e] \{\phi^e\} \\
& + [K_{i\psi}^e] \{\psi^e\} = \{F_{i,m}^e\} + \{F_{i\theta}^e\} \\
& [K_{ir}^e]^T \{d_i^e\} + [K_{rr}^e] \{d_r^e\} + [K_{r\phi}^e] \{\phi^e\} \\
& + [K_{r\psi}^e] \{\psi^e\} = \{F_{r,m}^e\} + \{F_{r\theta}^e\} \\
& [K_{i\phi}^e]^T \{d_i^e\} + [K_{r\phi}^e]^T \{d_r^e\} - [K_{\phi\phi}^e] \{\phi^e\} \\
& - [K_{\phi\psi}^e] \{\psi^e\} = \{F_{\phi}^e\} - \{F_{\phi\theta}^e\} \\
& [K_{i\psi}^e]^T \{d_i^e\} + [K_{r\psi}^e]^T \{d_r^e\} - [K_{\psi\phi}^e]^T \{\phi^e\} \\
& - [K_{\psi\psi}^e] \{\psi^e\} = \{F_{\psi}^e\} - \{F_{\psi\theta}^e\}
\end{aligned} \tag{19}$$

where $\{F_{i\theta}^e\}$ and $\{F_{r\theta}^e\}$ are the thermal loads associated with translational and rotational degrees of freedom, respectively; $\{F_{\phi}^e\}$ and $\{F_{\psi}^e\}$ are the pyroelectric and pyromagnetic load vectors, respectively.

Results and discussion

In this section, the static and free vibration behavior of FG-METE plates is studied using the FE formulation derived in the earlier section. Numerical examples are discussed in detail to evaluate and analyze the static behavior of MEE plates subjected to various loading conditions such as uniform temperature rise, non-uniform temperature rise, electric field force, and magnetic field force. Furthermore, the study is extended to evaluate the free vibration characteristics of the fully coupled FG-METE plates. Also, comparison is made between the individual and coupled effects of PE phase, PM phase, and thermal properties on the natural frequency of FG-METE plates.

Validation of the FE formulation

The credibility of the present FE model to accurately predict the static and free vibration behavior of

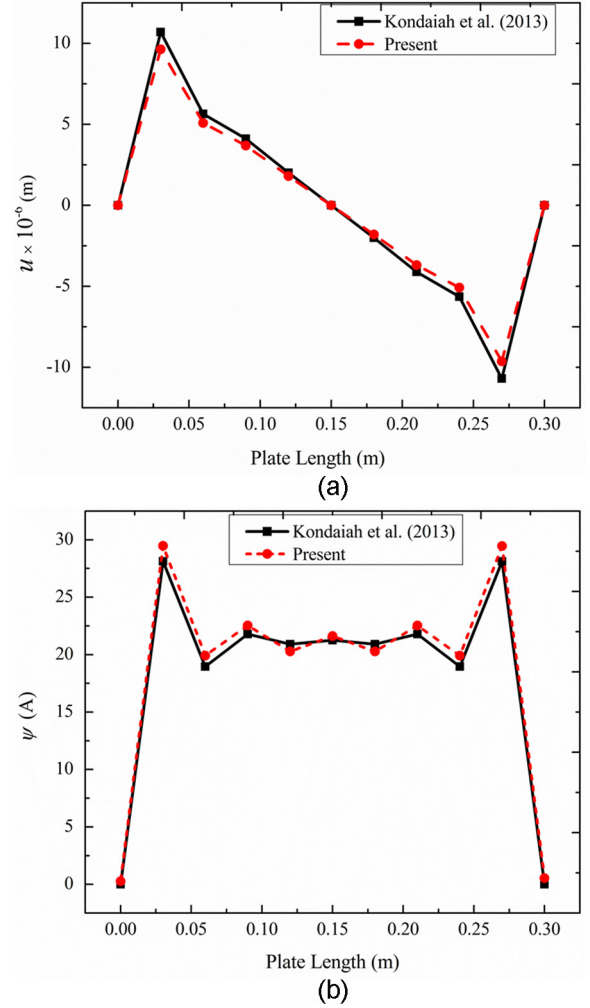


Figure 3. Validation plots of (a) displacement component u and (b) magnetic potential ψ of METE plate subjected to uniform temperature rise of 100 K.

FG-METE plates has been verified. An example of the multiphase MEE plate subjected to uniform temperature load, as considered by Kondaiah et al. (2013), is solved using the present FE formulation. It can be observed from Figure 3(a) and (b) that the results are correlated with each other. In addition, for the mechanical loading condition, the present formulation is validated with the results reported by Moita et al. (2009). It can be observed from Figure 4(a) to (c) that the present numerical formulation displays a close agreement with Moita et al. (2009). Thus, the present FE formulation can be extended to other forms of loading which are discussed in the subsequent sections. Meanwhile, the validation is extended for the case of free vibration response by comparing the results with the two instances of MEE plate analysis available in the literature. The material properties corresponding to various volume fractions of BaTiO_3 and CoFe_2O_4 are tabulated in Table 1. At first, for a simply supported $P/M/M/P$ -

Table 1. Material properties of BaTiO₃-CoFe₂O₄ composite with respect to different volume fractions, V_f , of BaTiO₃-CoFe₂O₄ (Kondaiah et al., 2012).

Material property	Material constants	0 V_f	0.2 V_f	0.4 V_f	0.5 V_f	0.6 V_f	0.8 V_f	1 V_f
Elastic constants (GPa)	$C_{11} = C_{22}$	286	250	225	220	200	175	166
	C_{12}	173	146	125	120	110	100	77
	$C_{13} = C_{23}$	170	145	125	120	110	100	78
	C_{33}	269.5	240	220	215	190	170	162
	$C_{44} = C_{55}$	45.3	45	45	45	45	50	43
	C_{66}	56.5	52	50	50	45	37.5	44.5
Piezoelectric constants (C/m ²)	e_{31}	0	-2	-3	-3.5	-3.5	-4	-4.4
	e_{33}	0	4	7	9.0	11	14	18.6
	e_{15}	0	0	0	0	0	0	11.6
Dielectric constant (10^{-9} C ² /N m ²)	$\eta_{11} = \eta_{22}$	0.08	0.33	0.8	0.85	0.9	1	11.2
	η_{33}	0.093	2.5	5	6.3	7.5	10	12.6
Magnetic permeability (10^{-4} N s ² /C ²)	$\mu_{11} = \mu_{22}$	-5.9	-3.9	-2.5	-2.0	-1.5	-0.8	0.05
	μ_{33}	1.57	1.33	1	0.9	0.75	0.5	0.1
Piezomagnetic constants (N/Am)	q_{31}	580	410	300	350	200	100	0
	q_{33}	700	550	380	320	260	120	0
	q_{15}	560	340	220	200	180	80	0
Magneto-electric constant (10^{-12} N s/VC)	$m_{11} = m_{22}$	0	2.8	4.8	5.5	6	6.8	0
	m_{33}	0	2000	2750	2600	2500	1500	0
Pyroelectric constant (10^{-7} C/m ² K)	p_2	0	-3.5	-6.5	-7.8	-9	-10.8	0
Pyromagnetic constant (10^{-5} C/m ² K)	τ_2	0	-36	-28	-23	-18	-8.5	0
Thermal expansion coefficient (10^{-6} K ⁻¹)	$\alpha_1 = \alpha_2$	10	10.8	11.8	12.3	12.9	14.1	15.7
	α_3	10	9.3	8.6	8.2	7.8	7.2	6.4
Density (kg/m ³)	ρ	5300	5400	5500	5550	5600	5700	5800

Table 2. Natural frequency for P/M/M/P-stacked MEE plate.

Mode	Lage et al. (2005)	Moita et al. (2009)	Present
1	2542.9	2449.7	2432.2
2	6391	6280.6	6268.4
3	6391	6280.6	6268.4
4	10,192	10,461.5	10,316.1

MEE: magneto-electro-elastic.

stacked METE square plate ($L = 1$ m, $H = 0.04$ m), the results obtained by the present code are analogous with Moita et al. (2009) and Lage et al. (2005), as tabulated in Table 2. In addition, the normalized frequencies of a simply supported P/M/P MEE plate ($L = 1$ m and $H = 0.3$ m) are validated. Table 3 compares the result ($\omega_n = \omega(L^2/H\sqrt{\rho/C_{11}})$, $\rho = 1600$ kg/m³) obtained using present numerical code and that reported by Moita et al. (2009). It can be observed from this table that the results are agreeing with Moita et al. (2009). Furthermore, the convergence of the natural frequency results with mesh refinement is explicitly depicted in Table 4. Hence, we can conclude that the present FE formulation can dependably produce results for various conditions of METE plate.

Static analysis

In this section, the static behavior of METE plate when subjected to various loading forms such as uniform

Table 3. Normalized frequencies ($\omega_n = \omega(L^2/H\sqrt{\rho/C_{11}})$) for simply supported pure P/M/P plate: $L = 1$ m; $H = 0.3$ m.

Mode	Moita et al. (2009)	Present
1	4.262	4.342
2	8.312	8.211
3	8.592	8.689
4	11.521	11.463
5	11.521	11.463
6	12.655	12.726

temperature loading, sinusoidal temperature loading, electric field force, and magnetic field force is analyzed. The direct and derived quantities are determined for the conventional three-layered METE plate (PMP and MPM) and FG-METE (FG-PMP and FG-MPM) plate. Also, an attention has been paid to investigate the influence of pyroeffects on the METE plates. The effect of stacking sequence, geometrical parameters such as boundary conditions, aspect ratio (a/b ratio), and the length-to-thickness ratio (a/h) is analyzed using the FE formulation derived in the preceding section.

Effect of uniform temperature rise. The static analysis of SSSS METE plate subjected to uniform temperature rise ($T = T_0$) is carried out. From Figure 5(a), it can be observed that FG-METE plate results in a lesser stress than the conventional three-layered METE plate. The through-thickness variations of magnetic flux density

Table 4. Convergence of the natural frequency of MEE plate with mesh size.

Mode no.	Mesh size				Moita et al. (2009)
	4 × 4	6 × 6	8 × 8	10 × 10	
1	2422.14	2428.60	2432.14	2432.21	2449.7
2	6255.74	6264.67	6268.31	6268.40	6280.6
3	6255.74	6264.67	6268.31	6268.40	6280.6
4	10,306.52	10,313.28	10,316.01	10,316.1	10,461.5

MEE: magneto-electro-elastic.

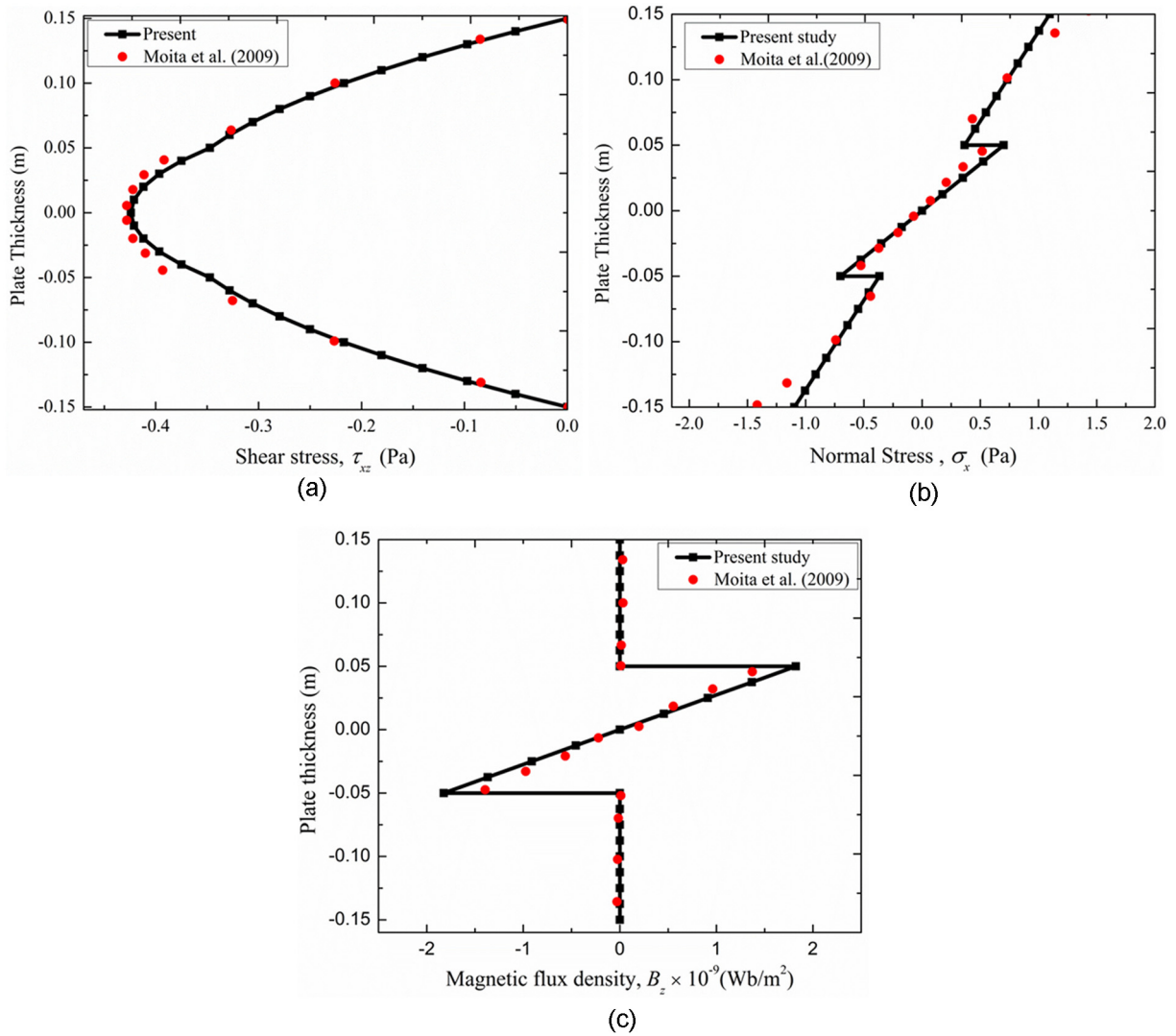


Figure 4. Validation plots of (a) shear stress, (b) normal stress, and (c) magnetic flux density.

and electric displacement are plotted in Figure 5(b) and (c), respectively. From these figures, it can be noticed that magnetic flux density (B_z) and electric displacement (D_z) are zero at the pure PM and pure PE phases of the corresponding stacking sequences, respectively. In addition, the variations of longitudinal displacement

component u , transverse displacement component w , electric potential ϕ , and magnetic potential ψ along the plate length ($y = 0.5 L$ and $x = 0$ to L) are shown in Figure 6(a) to (d), respectively. A negligible variation in the distribution of u is noticed for all the stacking sequences. It can be observed from Figure 6(a) that

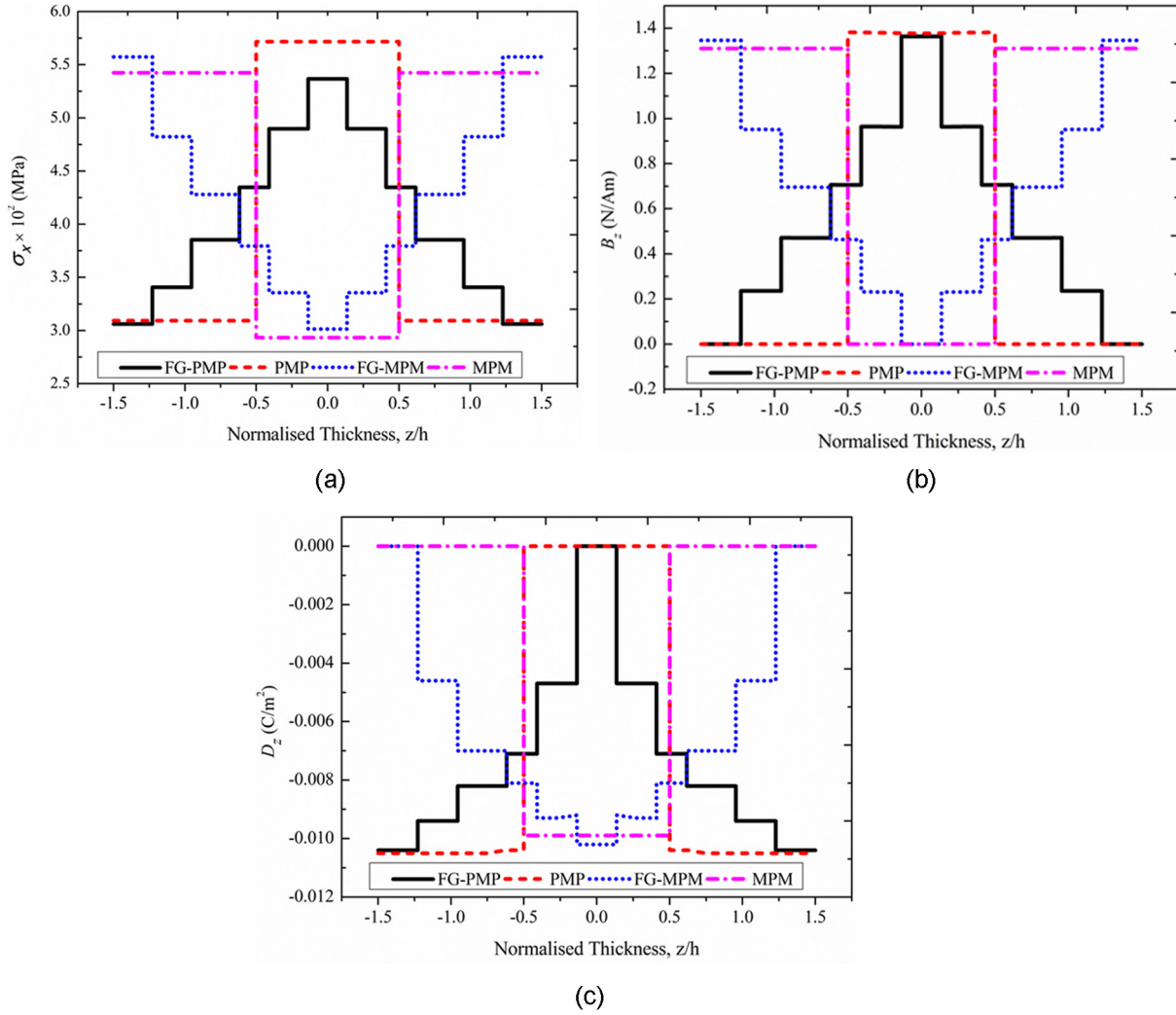


Figure 5. Variations of the (a) normal stress σ_x , (b) magnetic induction B_z , and (c) electric displacement D_z , across the plate thickness of METE plate subject to uniform temperature rise.

u_x is zero at the midspan, whereas the transverse deflection w is maximum at the midspan, as illustrated in Figure 6(b). In comparison with conventional three-layered METE plate, FG-METE plate displays a higher central deflection. The *FG-MPM* METE plate exhibits a higher electric potential, while *FG-MPM* METE plate results in a higher magnetic potential. Also, the magnetic potential and the electric potential are zero at both the edges and become constant along the length of the plate.

Effect of non-uniform temperature rise. The static response of METE plate exposed to the sinusoidal temperature field is evaluated. The temperature distribution can be represented as follows

$$T(x, y, z) = f(z)\bar{T}(x, y) \quad (20a)$$

where

$$f(z) = T_0 \text{ and } \bar{T}(x, y) = \sin \frac{\pi x}{a} \sin \frac{\pi y}{b} \quad (20b)$$

From Figure 7(a), it can be observed that the stress developed is lesser compared to the uniform temperature loading for the same magnitude of T_0 . The variation of B_z and D_z across the thickness of the plate is depicted in Figure 7(b) and (c), respectively. It can be noticed from Figure 7(b) and (c) that the displacement component u is marginally higher for *PMP* METE plate than the other stacking sequences. The central deflection w of METE plate subjected to sinusoidal temperature loading follows a similar variation trend as that of the uniform temperature rise (Figure 6(a)). The electric and magnetic potential is observed to be maximum at the midlength of the plate, while it is zero at the edges. It may be attributed to the temperature distribution considered for the analysis. From Figure 8(a) and (b), it can also be noticed that the magnitude of the displacement (u) and center deflection (w) are

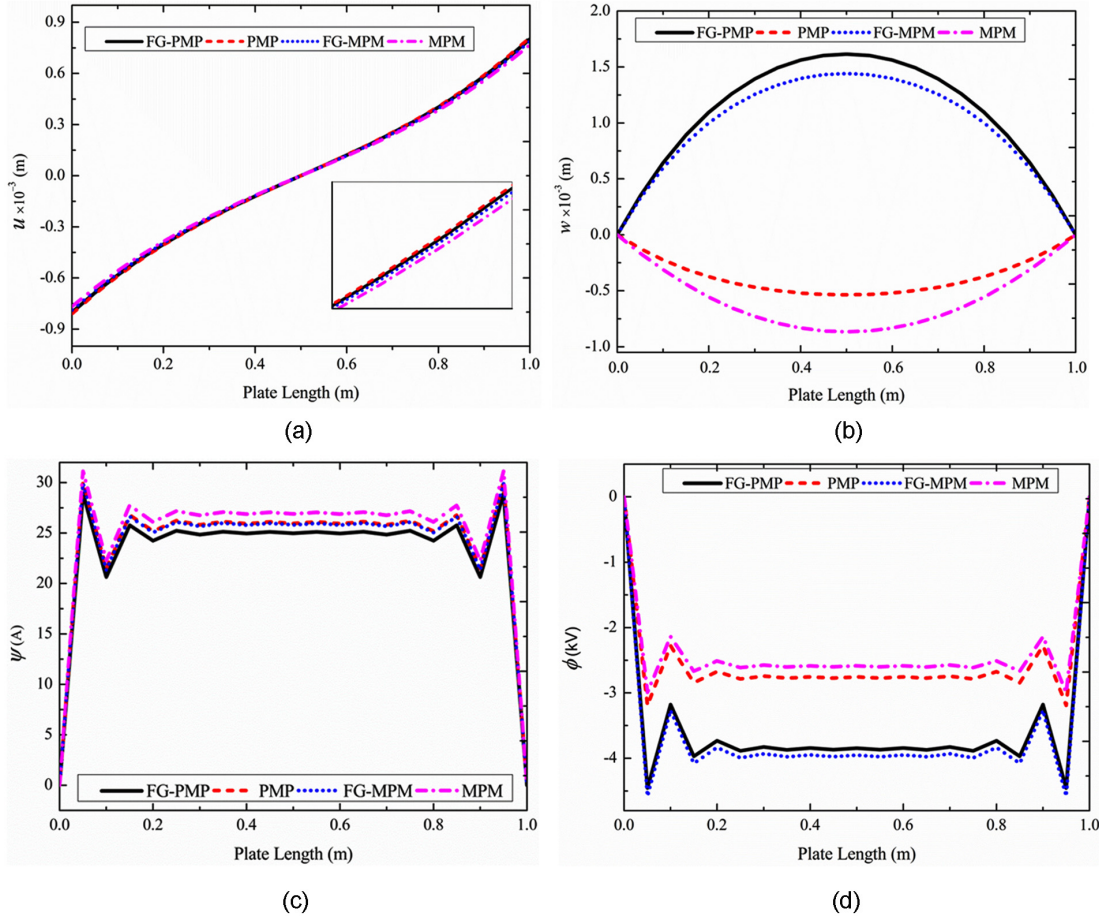


Figure 6. Variations of (a) displacement u , (b) center deflection w , (c) magnetic potential ψ , and (d) electric potential ϕ , along plate length of the simply supported METE plate subject to uniform temperature rise.

lower than the uniform temperature profile. In addition, *FG-MPM* METE plate has a predominant effect on both magnetic and electric potentials, as depicted in Figure 8(c) and (d), respectively.

Effect of electric field force. The variation of the static parameters of *FG-METE* plate and conventional three-layered METE plate under the influence of electric field force F_e is considered for the analysis. It can be noted that the electric field force is applied along the thickness direction alone. Figure 9(a) and (b) illustrates the distribution of normal stress and magnetic flux density across the plate thickness. The negative in-plane stress (σ_x) in Figure 9(a) indicates that the plate is under compression at a particular location of interest. From Figure 9(b), it is observed that the magnitude of magnetic induction B_z is insignificant in the top and the bottom layers of *FG-PMP* METE plate. It may be accounted to the presence of pure PE phase at the top and the bottom layers. Furthermore, B_z rises to the maximum at the middle layer composed of pure PM phase. This explanation holds good for conventional METE plate also. It can be

noticed from Figure 9(c) that the D_z varies linearly in each pure PE phase. In addition, the electric displacement D_z has a negligible value at the top and the bottom layers. It gradually increases till the middle layer where it drastically falls to zero due to the presence PM phase. The maximum D_z is noticed for *FG-MPM* stacking sequences at the mid-layer composed of pure PE phase. Unlike the temperature loading, a noticeable discrepancy exists with respect to displacement component u along the plate length, as shown in Figure 10(a). It can also be observed that the displacement component u is the maximum at the clamped end and it varies almost linearly along the plate length. The central deflection w is the minimum for *MPM* METE plate, whereas it is the maximum for *FG-MPM* METE plates, as shown in Figure 10(b). The magnetic potential (ψ) and electric potential (ϕ) are the maximum near clamped end and attain constant values over the plate length, as depicted in Figures 10(c) and (d), respectively. The *FG-METE* plates have an almost similar variation. However, the least variation is observed for conventional *MPM* METE plate.

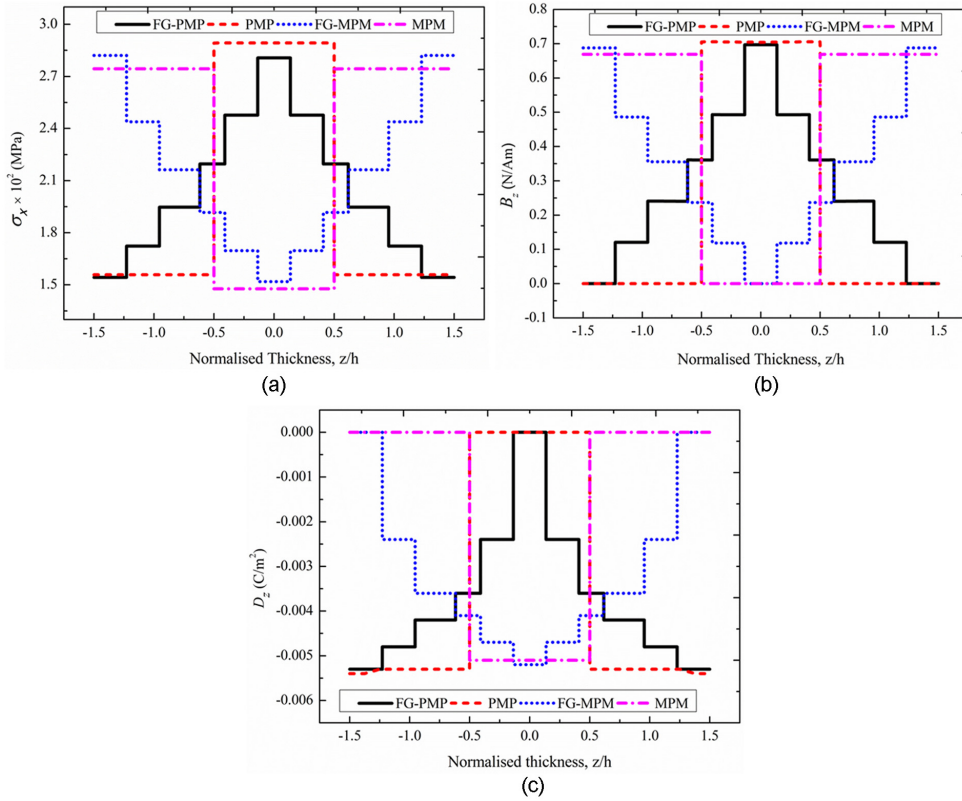


Figure 7. Variations of the (a) normal stress σ_x , (b) magnetic induction B_z , and (c) electric displacement D_z , across the plate thickness for METE plate subject to non-uniform temperature rise.

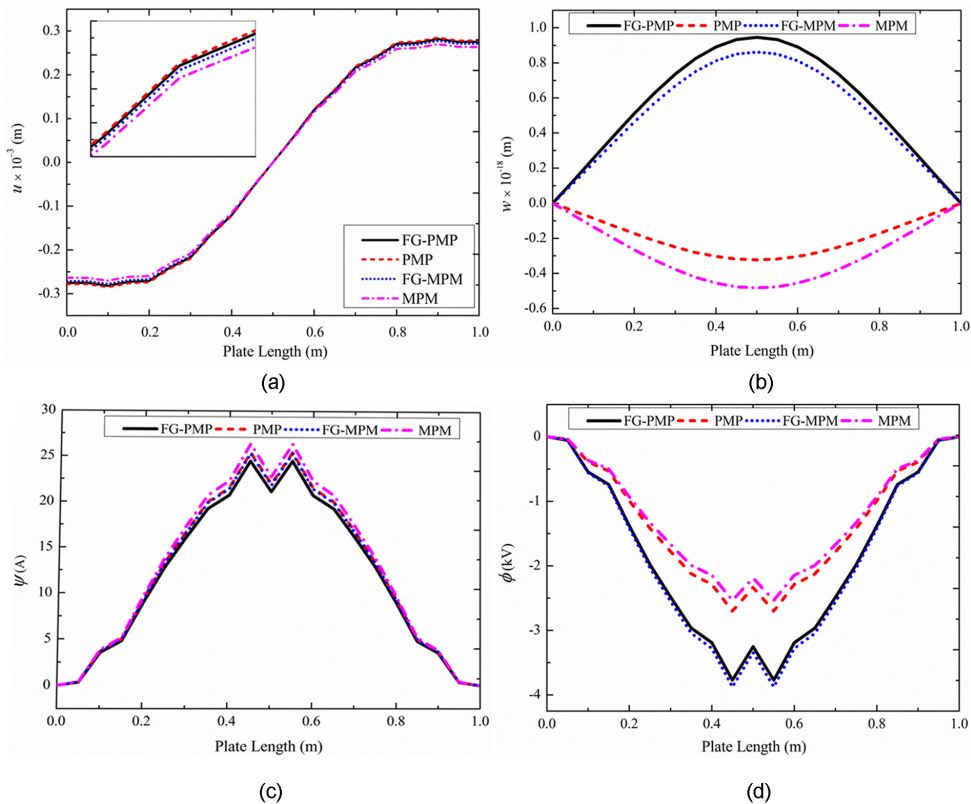


Figure 8. Variations of (a) displacement u , (b) center deflection w , (c) magnetic potential ψ , and (d) electric potential ϕ , along plate length of METE plate subject to non-uniform temperature rise.

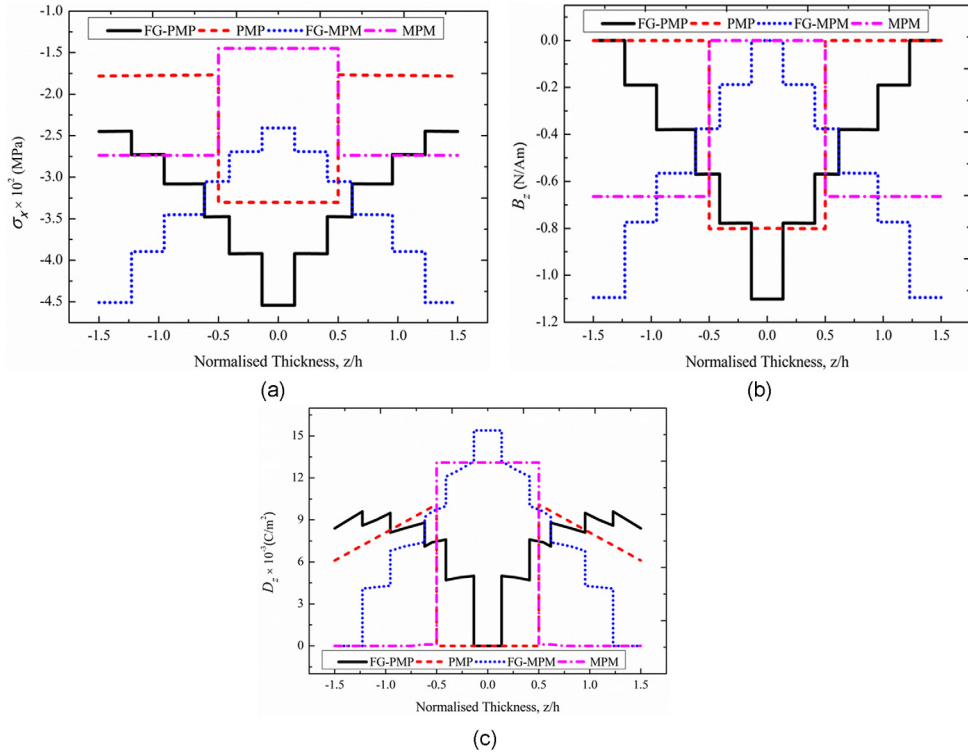


Figure 9. Variations of the (a) normal stress σ_x , (b) magnetic induction B_z , and (c) electric displacement D_z , across the plate thickness for METE plate subject to electric field force.

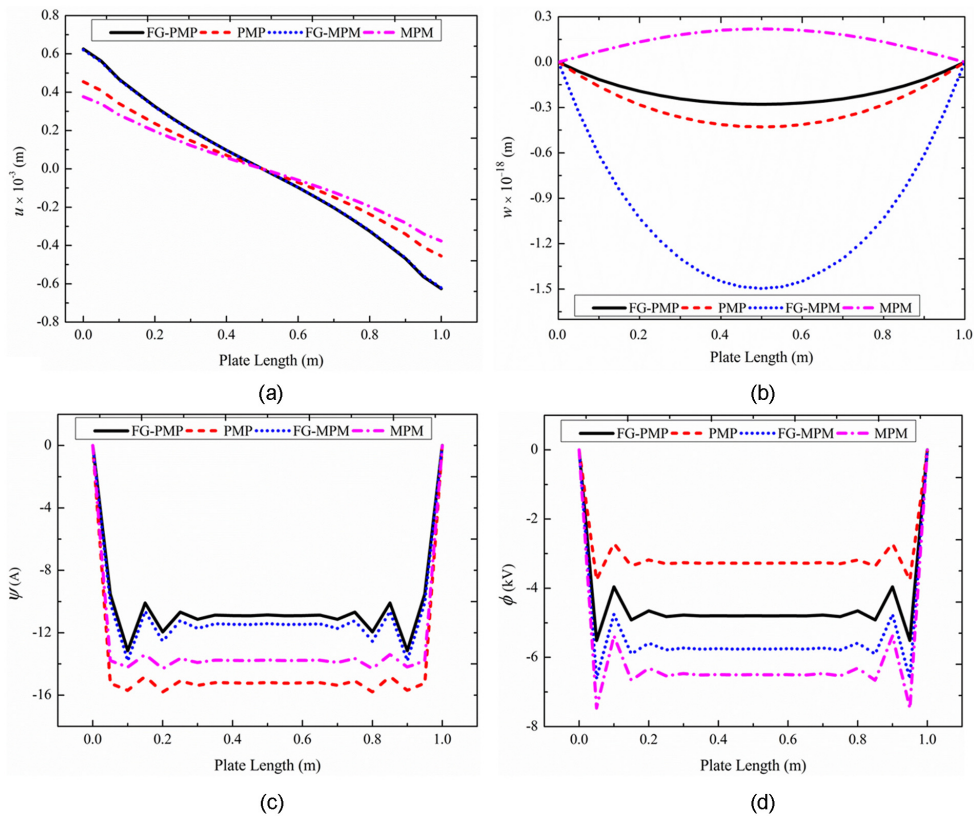


Figure 10. Variations of (a) displacement u , (b) center deflection w , (c) magnetic potential ψ , and (d) electric potential ϕ , along plate length of the METE plate subject to electric field force.

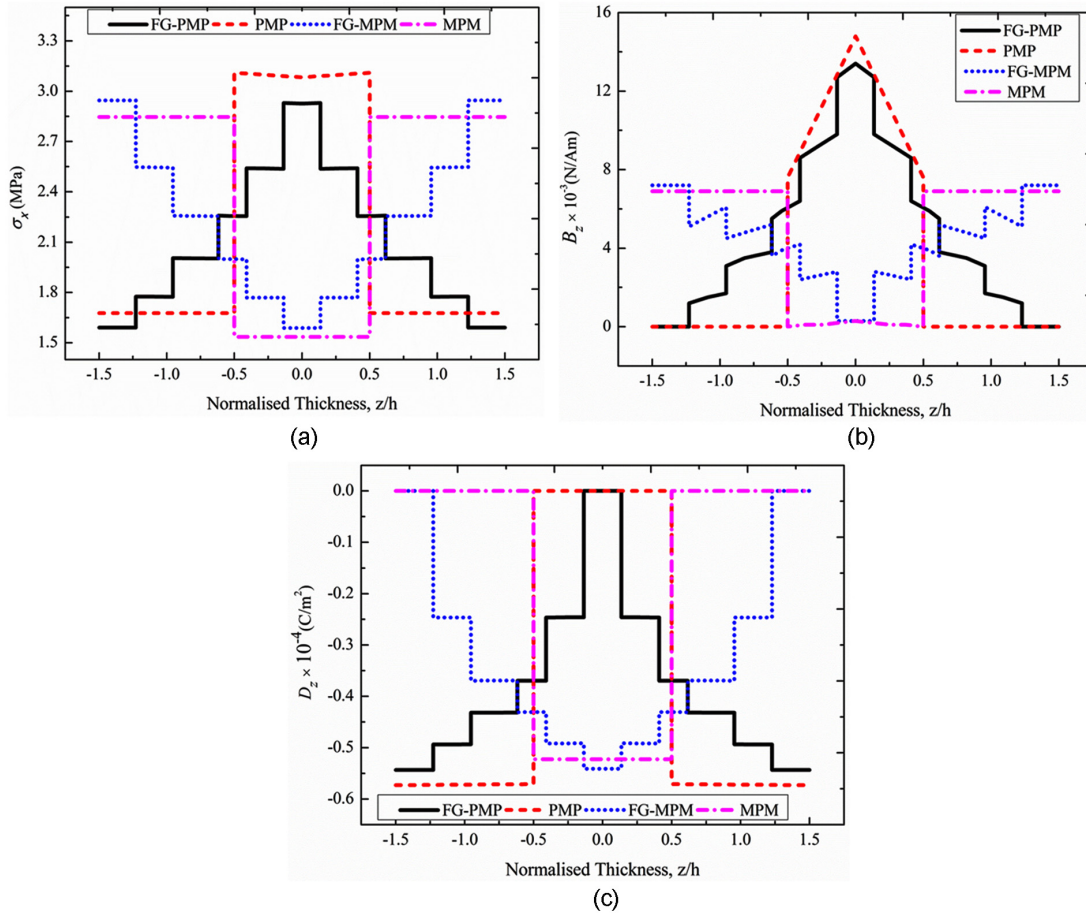


Figure 11. Variations of the (a) normal stress σ_x , (b) magnetic induction B_z , and (c) electric displacement D_z across the plate thickness for METE plate subject to magnetic field force.

Effect of magnetic field force. In this study, analogous to the electric field, the magnetic field force has been considered for the analysis, while the other conditions remain invariant. From Figure 11(a), it can be observed that the stress variation follows a similar trend as that of the electric loading. The magnetic flux density B_z varies almost linearly across the thickness of each layer except at the pure PE phase, as illustrated in Figure 11(b). The *FG-PMP* plate shows an increasing trend with the maximum values appearing at the mid-plane, while *FG-MPM* plate exhibits a decreasing trend. Furthermore, the maximum B_z is attained by three-layered *PMP* METE plate. Figure 11(c) depicts the variation of electric displacement component D_z across the thickness of different types of plates considered. A negligible variation with respect to u along the plate length is noticed for all the stacking sequences, as shown in Figure 12(a). Similarly, from Figure 12(b), it is observed that *FG-MPM* plate experiences more central deflection, while it is the minimum in three-layered *MPM* METE plate. The variation of electric potential is depicted in Figure 12(c). It can be noticed from this figure that the maximum value is obtained at the edges

and it remains almost constant along the plate length. In addition, from Figure 12(d), it can be seen that *PMP* stacking sequence has a prominent effect on the magnetic potential, while *MPM* METE plate results in a comparatively lesser magnetic potential.

Effect of combined loading. The combined effect of thermal, electric, and magnetic field forces is evaluated. The uniform temperature rise of 100 K, electric force of 10 C/m², and the magnetic force of 10 T (Tesla) are considered for the analysis. Figure 13(a) to (c) illustrates the distribution of normal stress σ_x , magnetic flux density B_z , and electric displacement component D_z , respectively. It can be witnessed from these figures that the thermo-magnetic load has a substantial effect followed by electromagnetic loading. Furthermore, a marginal discrepancy exists between thermo-electric and thermo-electromagnetic loads. The variation of displacement component in x -direction displacement component u , transverse displacement component w , electric potential, and magnetic potential along the plate length is depicted in Figure 14(a) to (d), respectively. It can be observed that a thermo-magnetic load

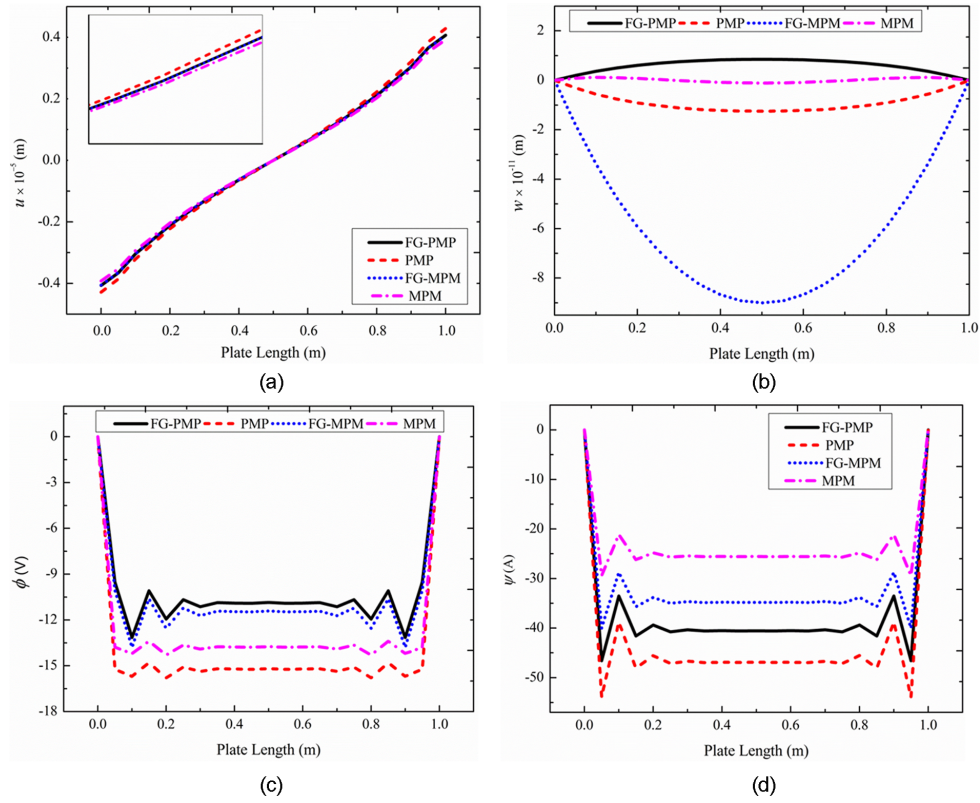


Figure 12. Variations of (a) displacement u , (b) center deflection w , (c) electric potential ϕ , and (d) magnetic potential ψ , along plate length of the METE plate subject to magnetic field force.

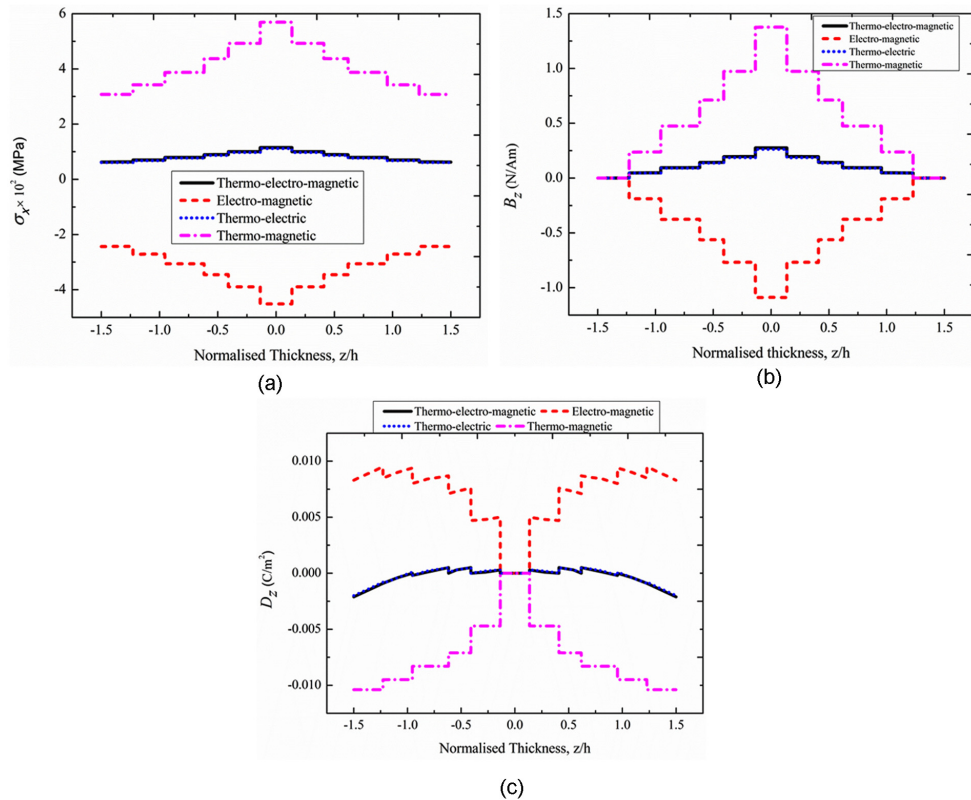


Figure 13. Influence of combined loads on (a) normal stress σ_x , (b) magnetic induction B_z , and (c) electric displacement D_z .

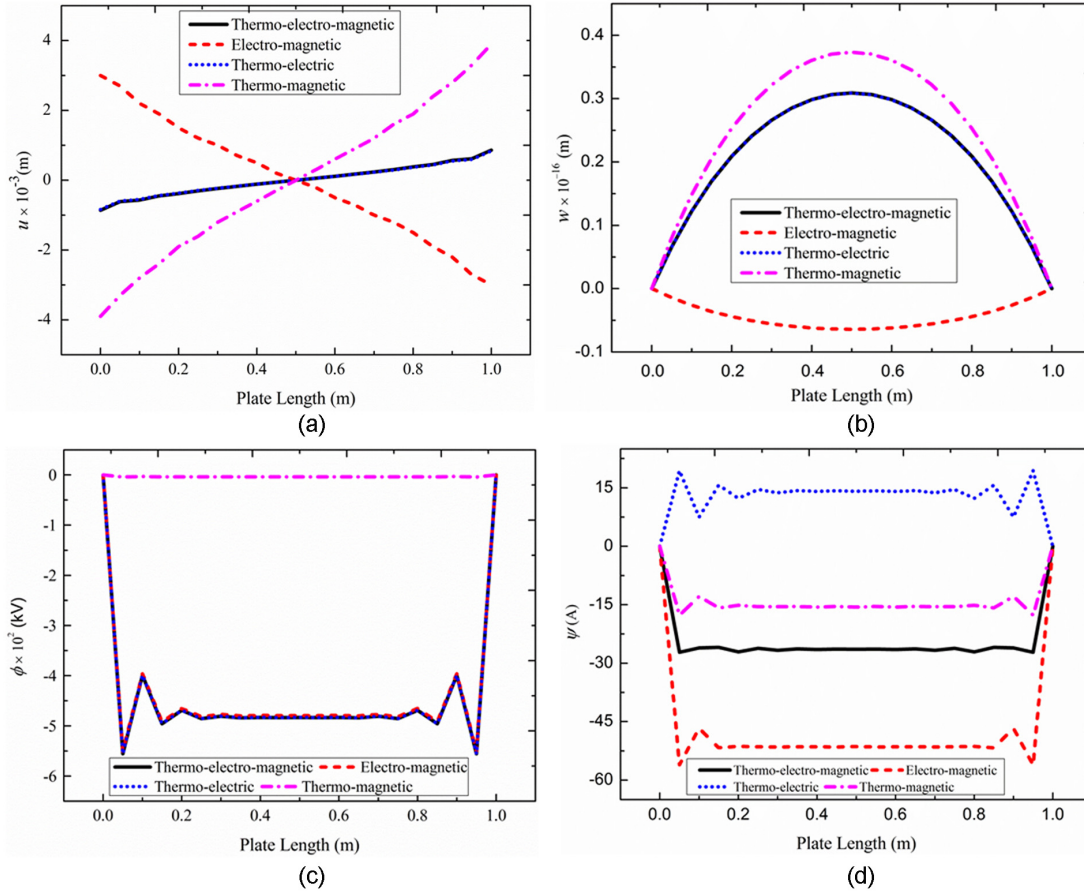


Figure 14. Influence of combined loads on (a) displacement u , (b) center deflection w , (c) electric potential ϕ , and (d) magnetic potential ψ of METE plate.

has a predominant influence on the displacement components. Furthermore, a significant effect of thermo-electric and electromagnetic loads is seen on the electric potential and magnetic potential, respectively.

Influence of pyroeffects. In the thermal environment, METE plate exhibits an additional coupling between thermal and electric and thermal and magnetic fields. This phenomenon is generally termed as pyrocoupling effects. The numerical investigation is carried out to evaluate the influence of pyroeffects on METE plates subjected to uniform and sinusoidal temperature loads. It is noticed that only the electric potential of the METE plate experiences a direct pyrocoupling effect. For both the stacking sequences, Figure 15(a) and (b) shows the influence of pyroeffects on the electric potential of FG-METE plate under uniform and sinusoidal temperature loads, respectively. It can be deduced from these figures that the pyroeffects tend to improve the electric potential of the METE plate for both forms of temperature loads.

Effect of boundary conditions. The distribution of direct and derived quantities with respect to various

boundary conditions is investigated. The various boundary conditions employed in the present analysis are given as follows

$$\begin{aligned}
 u = v = w = \theta_x = \theta_y = 0 & \text{ for clamped edge}(C) \\
 u = v = w = \theta_x = \theta_y \neq 0 & \text{ for free edge}(F) \\
 u \neq 0; v = w = \phi = \psi = 0 & \text{ at } x = 0, L \\
 u \neq 0; v = w = \phi = \psi = 0 & \text{ at } y = 0, b, \\
 & \text{for simply supported edge}(S)
 \end{aligned} \tag{21}$$

Figure 16(a) to (c) illustrates the comparison of the variation of magnetic flux density, normal stress (σ_x), and electric displacement, respectively, for different boundary conditions. It can be seen from these figures that the *CFFF* boundary condition has a predominant effect due to more number of free edges, while the *CCCC* boundary condition has a negligible effect. In addition, for the *CCFF* and *CFFF* boundary conditions, the maximum value of direct quantities is noticed at the free end, as shown in Figure 17(a) to (d). This may be due to asymmetric boundary conditions. For the symmetric boundary conditions (namely, *CCCC*, *SSSS*, and *CSCS*), the maximum central deflection w is noticed at the midspan of the plate. The longitudinal

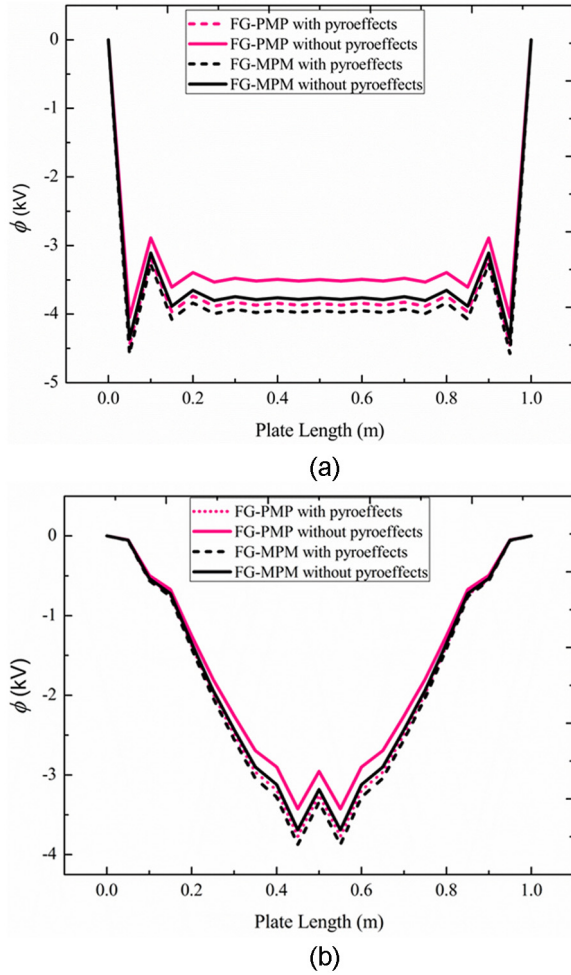


Figure 15. Influence of pyroeffects: (a) uniform temperature loads and (b) sinusoidal temperature loads.

displacement component u for the *CSCS* and *CFCF* METE plates varies symmetrically along the plate length. The electric potential and the magnetic potential are plotted in Figure 17(c) and (d), respectively. For the *SSSS* METE plate, the electric potential ϕ and magnetic potential ψ remain constant along the plate length with the maximum values appearing at the edges. Furthermore, for the *CFCF* and *CSCS* METE plates, the maximum ϕ and ψ are observed at the

midlength of the plate. In addition, *CFCF* METE plate results in a marginally higher value of ϕ and ψ in comparison with *CSCS* boundary condition. However, for the *CCSS* METE plate ϕ and ψ gradually increases from the clamped end to simply supported end.

Effect of aspect ratio (a/b) and length-to-thickness ratio (a/h). The numerical study is carried out to compute the effect of aspect ratio (a/b) and the length-to-thickness ratio (a/h) on the displacement components considering the *SSSS* boundary condition. The displacement components directly affect all the static parameters. Therefore, the study of the effect of a/h and a/b ratio is limited to displacement components. From Figure 18(a) and (b), it can be noticed that with the increase in aspect ratio, the displacement components increase. Similarly, the variation in the displacement components is proportional to the length-to-thickness ratio (a/h), as illustrated in Figure 19(a) and (b).

Free vibration analysis of FG-METE plate: evaluation of effect of coupling factors

Free vibration analysis of METE plate is carried out by considering full coupling of the thermal field with magnetic, electric, and elastic fields. The effect of METE coupling, the electric effect of PE phase, magnetic effect of PM phase, and the effect of thermal constants on the natural frequencies are individually investigated. In this regard, the equivalent stiffness matrices $[K_{eq}]$, $[K_{eq_elastic}]$, $[K_{eq_\phi\phi}]$, $[K_{eq_|\psi\psi}]$, and $[K_{eq_|\theta\theta}]$ for each case are derived as illustrated in Appendix 2. Table 5 encapsulates the description and significance of the different frequencies computed along with the corresponding stiffness matrices. Furthermore, the effect of stacking sequence is studied by considering two forms of ply arrangement, namely, *FG-PMP* and *FG-MPM* METE plates.

Case 1: simply supported on all edges (SSSS). For a simply supported plate, following constraints are enforced

Table 5. Different stiffness matrices.

Stiffness matrix symbol	Related frequency	Description	Significance
$[K_{eq}]$	f_{eq}	Stiffness matrix for fully coupled magneto-thermo-electro-elastic material	Effect of coupled fields
$[K_{elastic}]$	$f_{elastic}$	Stiffness matrix neglecting coupling effects	Effect of elastic constants only
$[K_{eq_ \phi\phi}]$	$f_{ \phi\phi}$	Stiffness matrix considering piezoelectric effect	Effect of piezoelectric phase
$[K_{eq_ \psi\psi}]$	$f_{ \psi\psi}$	Stiffness matrix considering piezomagnetic effect	Effect of piezomagnetic phase
$[K_{eq_ \theta\theta}]$	$f_{ \theta\theta}$	Stiffness matrix considering thermal effect	Effect of thermal constants

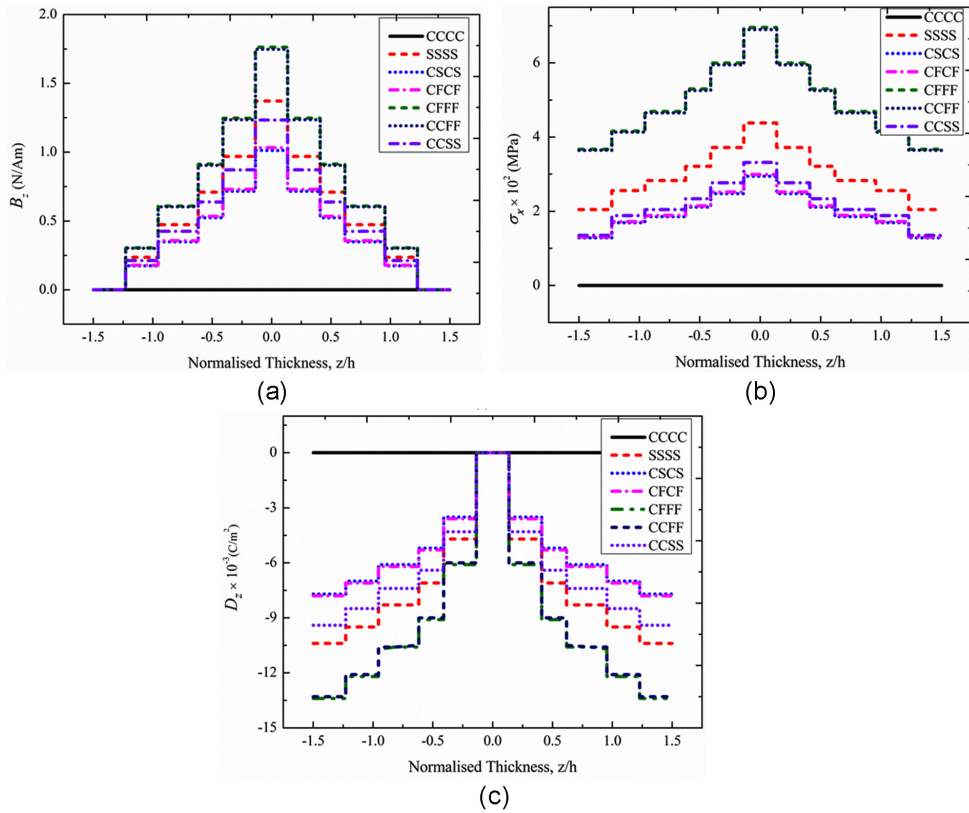


Figure 16. Effect of boundary condition on (a) magnetic field density, (b) normal stress— σ_x , and (c) electric displacement.

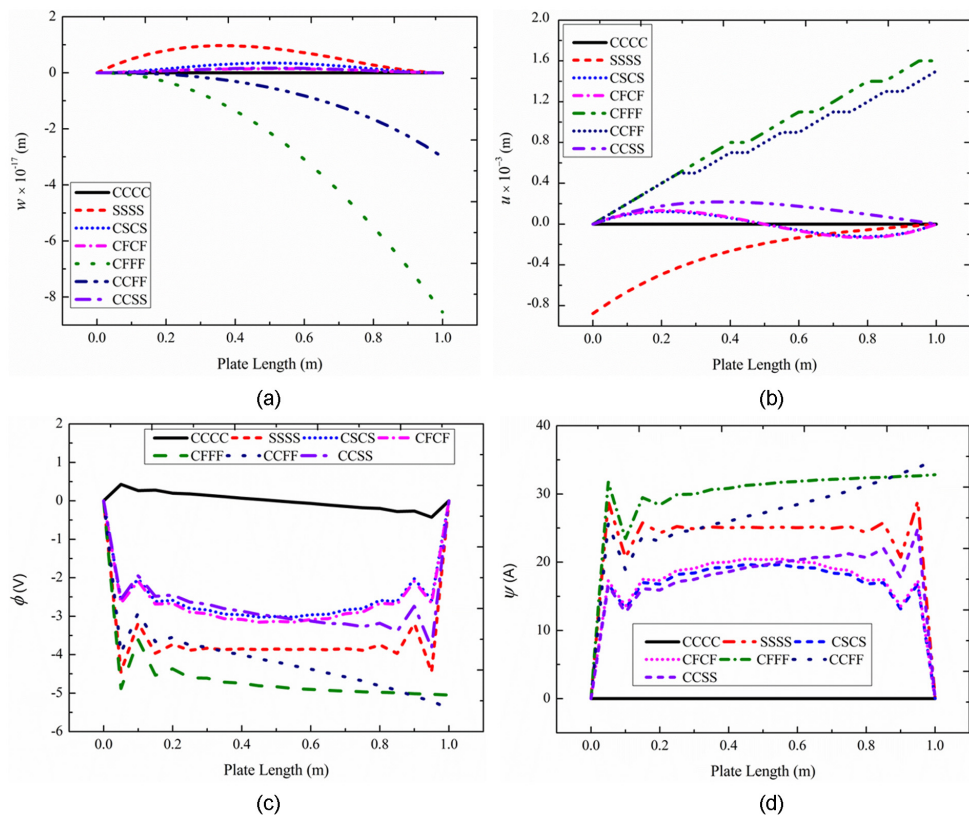
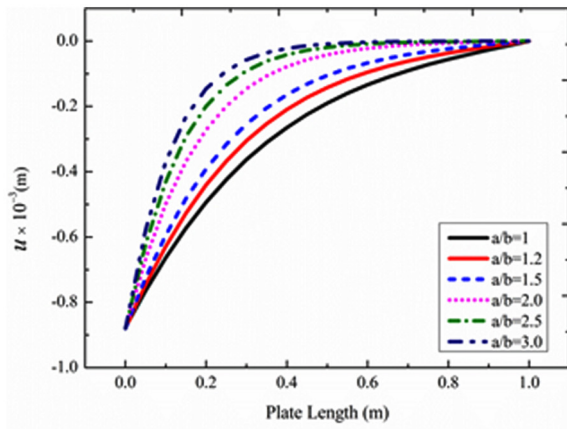


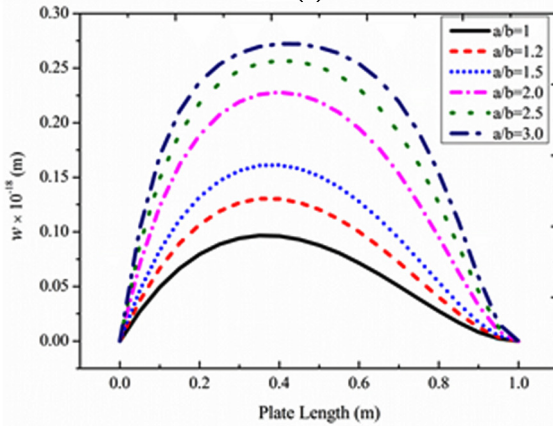
Figure 17. Effect of boundary condition on (a) transverse deflection w , (b) longitudinal displacement component u , (c) electric potential, and (d) magnetic potential.

Table 6. Natural frequencies (rad/s) for SSSS FG-METE plate: $L = 1$ m; $H = 0.04$ m.

Mode number	Simply supported condition									
	FG-PMP					FG-MPM				
	f_{eq}	$f_{elastic}$	$f_{\varphi\varphi}$	$f_{\psi\psi}$	$f_{\theta\theta}$	f_{eq}	$f_{elastic}$	$f_{\varphi\varphi}$	$f_{\psi\psi}$	$f_{\theta\theta}$
1	1303.87	1303.72	1303.91	1303.72	1303.64	1550.22	1550.20	1550.25	1550.21	1550.16
2	5546.78	5544.76	5547.07	5544.48	5544.74	6428.41	6427.36	6428.89	6426.81	6427.37
3	7204.42	7202.89	7204.59	7202.81	7202.91	8350.74	8349.98	8351.09	8349.81	8350.01
4	10,059.04	10,052.52	10,059.76	10,051.67	10,052.51	11,309.98	11,307.04	11,311.35	11,305.5	11,307.03
5	10,059.04	10,052.52	10,059.76	10,051.67	10,052.51	11,309.98	11,307.04	11,311.35	11,305.5	11,307.03
6	11,598.45	11,595.51	11,599.01	11,595.14	11,595.51	13,479.73	13,478.41	13,480.39	13,477.71	13,478.39
7	15,846.27	15,821.91	15,848.99	15,818.79	15,821.89	17,617.66	17,608.23	17,622.09	17,603.31	17,608.23
8	16,606.86	16,585.27	16,609.09	16,582.49	16,585.26	17,919.05	17,910.18	17,923.07	17,905.64	17,910.17



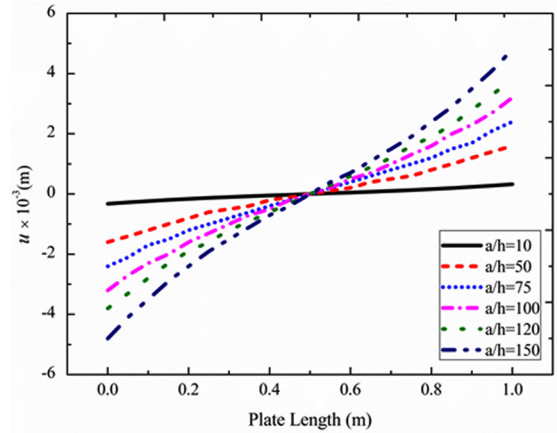
(a)



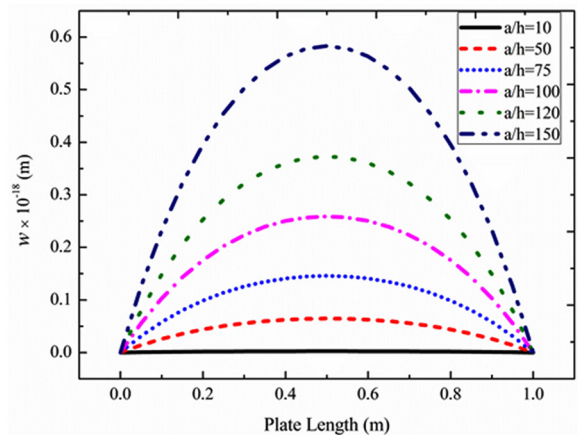
(b)

Figure 18. Effect of a/b ratio on (a) u and (b) w of METE plate subjected to uniform temperature load.

$$\begin{aligned}
 &u(x, y, 0) \text{ and } \theta_x = 0 \text{ at } y = 0 \text{ and } y = L \\
 &v(x, y, 0) = 0 \text{ and } \theta_y = 0 \text{ at } x = 0 \text{ and } x = L \\
 &w(x, y, 0) = 0 \text{ at } x = 0, x = L, y = 0 \text{ and } y = L \\
 &\phi(x, y, 0) = \psi(x, y, 0) = T(x, y, 0) = 0 \text{ at} \\
 &x = 0, x = L, y = 0 \text{ and } y = L
 \end{aligned} \quad (22)$$



(a)



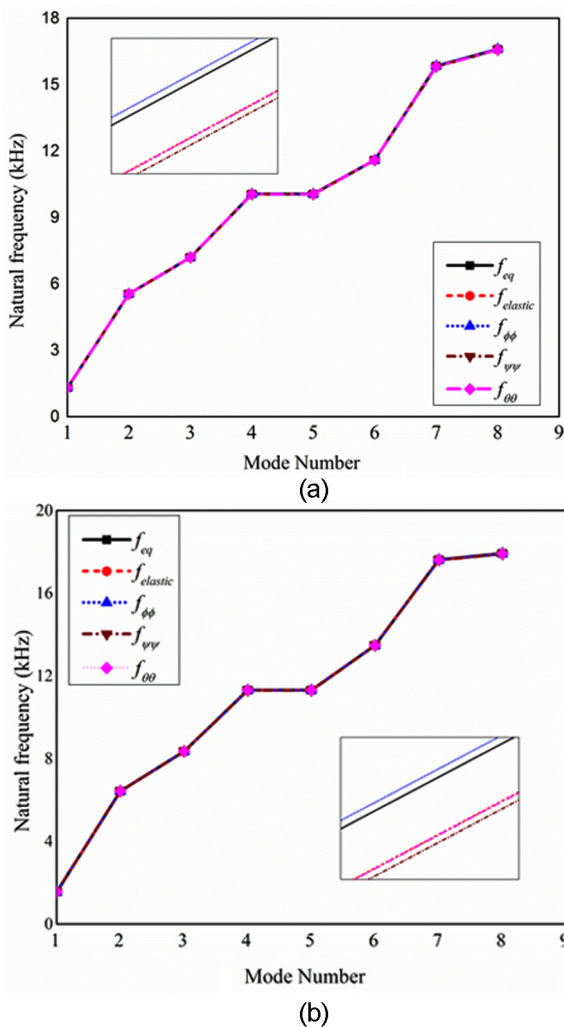
(b)

Figure 19. Effect of a/h ratio on (a) u and (b) w of METE plate subjected to uniform temperature load.

It can be noticed from Table 6 that the effect of coupling parameters on the natural frequency variations is significantly observed for higher modes with respect to both *FG-PMP* and *FG-MPM* stacking sequences. In comparison with $f_{elastic}$, the coupling effects (f_{eq}) tend to increase the frequency of the system. Also, it can be

Table 7. Natural frequencies for CCCC FG-METE plate: $L = 1$ m; $H = 0.04$ m.

Mode number	Clamped condition									
	FG-PMP					FG-MPM				
	f_{eq}	$f_{elastic}$	$f_{\varphi\varphi}$	$f_{\psi\psi}$	$f_{\theta\theta}$	f_{eq}	$f_{elastic}$	$f_{\varphi\varphi}$	$f_{\psi\psi}$	$f_{\theta\theta}$
1	2572.91	2571.88	2572.94	2571.76	2571.88	2975.81	2975.35	2976.01	2975.11	2975.74
2	8989.57	8974.86	8991.17	8973.01	8974.84	9795.74	9790.44	9798.26	9787.71	9795.43
3	12,651.33	12,648.94	12,651.56	12,648.63	12,648.96	13,451.57	13,450.46	13,452.07	13,449.91	13,451.4
4	18,040.12	18,035.24	18,040.69	18,034.62	18,035.23	19,359.84	19,357.83	19,360.78	19,356.82	19,359.83
5	18,040.12	18,035.24	18,040.69	18,034.62	18,035.23	19,359.84	19,357.83	19,360.78	19,356.82	19,359.83
6	21,065.42	20,361.18	21,058.74	20,361.05	21,063.87	21,312.58	20,790.54	21,302.81	20,790.4	21,312.41
7	22,898.11	21,000.39	22,890.38	21,000.39	22,897.38	24,098.89	21,262.26	24,084.48	21,258.95	24,098.71
8	28,079.23	22,861.37	28,067.19	22,856.73	28,078.78	28,419.88	24,086.48	28,411.94	24,080.15	28,419.72

**Figure 20.** Comparison of natural frequency: (a) FG-PMP and (b) FG-MPM METE plate—simply supported condition.

noticed from Table 6 that $f_{\psi\psi}$ and $f_{\theta\theta}$ are less than f_{eq} , while $f_{\phi\phi}$ is higher than f_{eq} . This suggests that a marginal dominance of $f_{\phi\phi}$ prevails for both the stacking sequences, and electric effect of PE phase increases the

frequency of the system. But the magnetic effect of PM phase along with thermal properties tends to deteriorate the system frequency. The same is graphically illustrated in Figure 20(a) and (b) for FG-PMP and FG-MPM stacking sequences, respectively.

Case 2: clamped on all edges (CCCC). In this case, all the degrees of freedom of the nodes lying at the edges are fully constrained. As illustrated in Table 7, for higher modes (mode no 6 and above), $f_{\theta\theta}$ is almost equal to f_{eq} . This is accounted to the predominant influence of thermal properties over PE and PM effect in clamped boundary condition. Hence, for both the stacking sequences, the inclusion of thermal properties increases the frequency of the plate at the higher modes, as shown in Figure 21(a) and (b).

Effect of boundary condition and stacking sequence on natural frequency. The effect of different boundary conditions on the natural frequency of METE plates is illustrated in Table 8. It can be noticed that for both the stacking sequences, namely, FG-PMP and FG-MPM, CCCC boundary condition results in a higher natural frequency. Comparatively, FG-MPM METE plate has a predominant effect on the natural frequency than FG-PMP METE plate. This may be attributed to the higher values of elastic constants of the magnetostrictive layer.

Conclusion

This article makes a first attempt to evaluate the effect of various coupled fields on the free vibration and static behavior of METE plates. A FE formulation is derived using Hamilton's principle and constitutive equations of METE solids. A full coupling between elastic, electric, magnetic, and thermal fields is considered. A comparative study has been made to investigate the effect of each coupling field and its associated stiffness matrices on free vibration characteristics of FG-METE

Table 8. Natural frequencies for METE plate: $L = 1$ m; $H = 0.04$ m.

Mode	Simply supported		Clamped-clamped		Clamped-free	
	FG-PMP	FG-MPM	FG-PMP	FG-MPM	FG-PMP	FG-MPM
1	1303.87	1550.22	2572.91	2975.81	1541.32	1786.85
2	5546.78	6428.41	8989.57	9795.74	4712.77	5337.23
3	7204.42	8350.74	12,651.33	13,451.57	5524.01	6355.67
4	10,059.04	11,309.98	18,040.12	19,359.84	9178.37	10,147.13
5	10,059.04	11,309.98	18,040.12	19,359.84	10,869.01	12,338.07
6	11,598.45	13,479.73	21,065.42	21,312.58	12,124.55	12,776.81
7	15,846.27	17,617.66	22,898.11	24,098.89	14,383.36	15,819.56
8	16,606.86	17,919.05	28,079.23	28,419.88	15,642.39	17,142.28

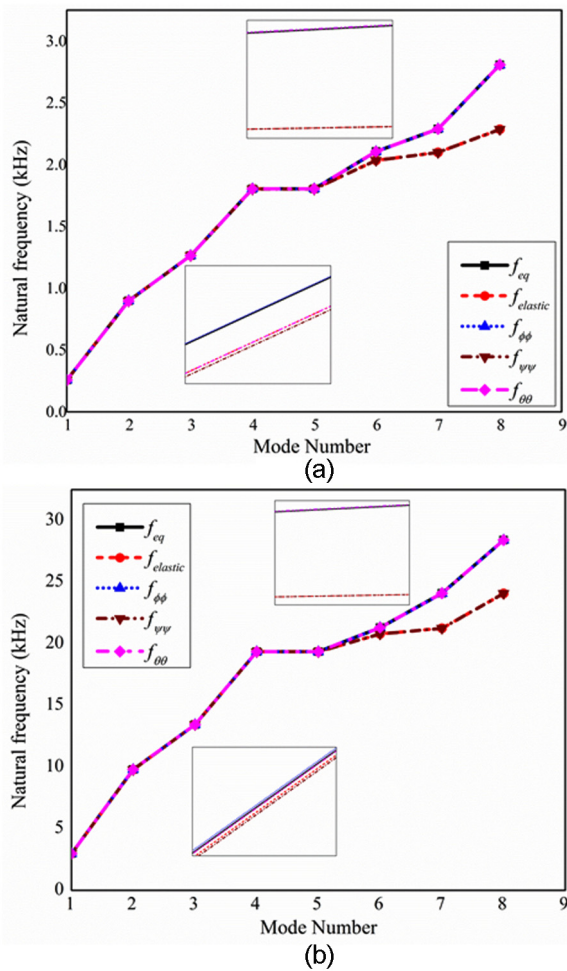


Figure 21. Comparison of natural frequency: (a) FG-PMP and (b) FG-MPM METE plate—clamped condition.

plate. The kinematics of the plate is assumed to follow first-order shear deformation theory. From the results, it is understood that the pure PE phase has a predominant effect on the natural frequency of METE plate. Through parametric studies, the influence of different boundary conditions and stacking sequence is explored. It is evident that for SSSS boundary condition, the magnetostrictive phase and the thermal properties

inclusion have negligible effects on the frequency of FG-METE plates, whereas for CCCC boundary condition, a significant effect of thermal properties on the natural frequency is noticed.

The FE formulation is simplified by considering partial coupling of the thermal field with the magnetic, electric, and elastic fields and static analysis of METE plate is carried out. The effect of temperature loads (uniform and non-uniform), electric loads, and magnetic loads on the static parameters of METE plate is examined. Also, the most significant load combination is investigated. In case of thermal loading, the numerical results suggest that the pyroeffects tend to improve the electric potential of the system. In contrast to the sinusoidal temperature load, uniform temperature loads have a predominant influence on the direct and derived quantities. This is attributed to the constant pyroloads generated. A comparative study of the influence of different boundary conditions reveals that asymmetric boundary condition (CFFF) has a prominent influence on the direct quantities. Meanwhile, increase in the aspect ratio (a/b) and length-to-thickness (a/h) ratio increases the displacement components. It is believed that this study can be very helpful for the understanding structural response of FG-METE plate subjected to various loading conditions.

Declaration of conflicting interests

The author(s) declared no potential conflicts of interest with respect to the research, authorship, and/or publication of this article.

Funding

The author(s) received no financial support for the research, authorship, and/or publication of this article.

References

Ahmad SN, Upadhyay CS and Venkatesan C (2006) Electro-thermo-elastic formulation for the analysis of smart structures. *Smart Materials and Structures* 15(2): 401.
 Alaimo A, Milazzo A and Orlando C (2013) A four-node MITC finite element for magneto-electro-elastic multi-layered plates. *Computers & Structures* 129: 120–133.

- Annigeri AR, Ganesan N and Swarnamani S (2007) Free vibration behavior of multiphase and layered magneto-electro-elastic beam. *Journal of Sound and Vibration* 299(1): 44–63.
- Benedetti I and Milazzo A (2017) Advanced models for smart multilayered plates based on Reissner mixed variational theorem. *Composites Part B: Engineering* 119: 215–229.
- Bhangale RK and Ganesan N (2006) Free vibration of simply supported functionally graded and layered magneto-electro-elastic plates by finite element method. *Journal of Sound and Vibration* 294(4): 1016–1038.
- Chen J, Chen H, Pan E, et al. (2007) Modal analysis of magneto-electro-elastic plates using the state-vector approach. *Journal of Sound and Vibration* 304(3): 722–734.
- Daga A, Ganesan N and Shankar K (2009) Behavior of magneto-electro-elastic sensors under transient mechanical loading. *Sensors and Actuators A: Physical* 150(1): 46–55.
- Ebrahimi F and Barati MR (2016a) Dynamic modeling of a thermo-piezo-electrically actuated nanosize beam subjected to a magnetic field. *Applied Physics: A* 122: 451.
- Ebrahimi F and Barati MR (2016b) Vibration analysis of smart piezoelectrically actuated nanobeams subjected to magneto-electrical field in thermal environment. *Journal of Vibration and Control*. Epub ahead of print 29 April. DOI: 10.1177/1077546316646239.
- Ebrahimi F and Salari E (2015) Thermal buckling and free vibration analysis of size dependent Timoshenko FG nanobeams in thermal environments. *Composite Structures* 128: 363–380.
- Gao Y, Xu B and Huh H (2010) Electromagneto-thermo-mechanical behaviors of conductive circular plate subject to time-dependent magnetic fields. *Acta Mechanica* 210(1): 99–116.
- Huang DJ, Ding HJ and Chen WQ (2007) Analytical solution for functionally graded magneto-electro-elastic plane beams. *International Journal of Engineering Science* 45(2): 467–485.
- Kattimani SC and Ray MC (2014a) Active control of large amplitude vibrations of smart magneto-electro-elastic doubly curved shells. *International Journal of Mechanics and Materials in Design* 10(4): 351–378.
- Kattimani SC and Ray MC (2014b) Smart damping of geometrically nonlinear vibrations of magneto-electro-elastic plates. *Composite Structures* 114: 51–63.
- Kattimani SC and Ray MC (2015) Control of geometrically nonlinear vibrations of functionally graded magneto-electro-elastic plates. *International Journal of Mechanical Sciences* 99: 154–167.
- Kondaiah P, Shankar K and Ganesan N (2012) Studies on magneto-electro-elastic cantilever beam under thermal environment. *Coupled System Mechanics* 1(2): 205–217.
- Kondaiah P, Shankar K and Ganesan N (2013) Pyroelectric and pyromagnetic effects on behavior of magneto-electro-elastic plate. *Coupled System Mechanics* 2(1): 1–22.
- Kumaravel A, Ganesan N and Sethuraman R (2007) Buckling and vibration analysis of layered and multiphase magneto-electro-elastic beam under thermal environment. *Multidiscipline Modeling in Materials and Structures* 3(4): 461–476.
- Kumaravel A, Ganesan N and Sethuraman R (2010) Buckling and vibration analysis of layered and multiphase magneto-electro-elastic cylinders subjected to uniform thermal loading. *Multidiscipline Modeling in Materials and Structures* 6(4): 475–492.
- Lage RG, Soares CM and Soares CA (2005) Static and free vibration analysis of magneto-electro-elastic laminated plates by a layerwise partial mixed finite element model. In: *The 3rd international conference on structural stability and dynamics*, Kissimmee, FL.
- Lage RG, Soares CM, Soares CA, et al. (2004) Layerwise partial mixed finite element analysis of magneto-electro-elastic plates. *Computers & Structures* 82(17): 1293–1301.
- Lee JL and Lin CB (2010) The magnetic viscous damping effect on the natural frequency of a beam plate subject to an in-plane magnetic field. *Journal of Applied Mechanics* 77(1): 011014.
- Milazzo A (2013) A one-dimensional model for dynamic analysis of generally layered magneto-electro-elastic beams. *Journal of Sound and Vibration* 332(2): 465–483.
- Milazzo A (2014a) Layer-wise and equivalent single layer models for smart multilayered plates. *Composites Part B: Engineering* 67: 62–75.
- Milazzo A (2014b) Refined equivalent single layer formulations and finite elements for smart laminates free vibrations. *Composites Part B: Engineering* 61: 238–253.
- Moita JMS, Soares CMM and Soares CAM (2009) Analyses of magneto-electro-elastic plates using a higher order finite element model. *Composite Structures* 91(4): 421–426.
- Oh J and Cho M (2004) A finite element based on cubic zig-zag plate theory for the prediction of thermo-electric-mechanical behaviors. *International Journal of Solids and Structures* 41(5): 1357–1375.
- Pan E (2001) Exact solution for simply supported and multilayered magneto-electro-elastic plates. *Journal of Applied Mechanics* 68(4): 608–618.
- Pan E and Heyliger PR (2002) Free vibrations of simply supported and multilayered magneto-electro-elastic plates. *Journal of Sound and Vibration* 252(3): 429–442.
- Panda S and Ray MC (2008) Active constrained layer damping of geometrically nonlinear vibrations of functionally graded plates using piezoelectric fiber-reinforced composites. *Smart Materials and Structures* 17(2): 025012.
- Panda S and Ray MC (2009) Active control of geometrically nonlinear vibrations of functionally graded laminated composite plates using piezoelectric fiber reinforced composites. *Journal of Sound and Vibration* 325(1): 186–205.
- Pérez-Fernández LD, Bravo-Castillero J, Rodri R, et al. (2009) On the constitutive relations and energy potentials of linear thermo-magneto-electro-elasticity. *Mechanics Research Communications* 36(3): 343–350.
- Phoenix SS, Satsangi SK and Singh BN (2009) Layer-wise modelling of magneto-electro-elastic plates. *Journal of Sound and Vibration* 324(3): 798–815.
- Ramirez F, Heyliger PR and Pan E (2006) Free vibration response of two-dimensional magneto-electro-elastic laminated plates. *Journal of Sound and Vibration* 292(3): 626–644.
- Ray MC and Shivakumar J (2009) Active constrained layer damping of geometrically nonlinear transient vibrations of composite plates using piezoelectric fiber-reinforced composite. *Thin-Walled Structures* 47(2): 178–189.
- Razavi S and Shooshtari A (2015) Nonlinear free vibration of magneto-electro-elastic rectangular plates. *Composite Structures* 119: 377–384.

- Shooshtari A and Razavi S (2015a) Large amplitude free vibration of symmetrically laminated magneto-electro-elastic rectangular plates on Pasternak type foundation. *Mechanics Research Communications* 69: 103–113.
- Shooshtari A and Razavi S (2015b) Linear and nonlinear free vibration of a multilayered magneto-electro-elastic doubly-curved shell on elastic foundation. *Composites Part B: Engineering* 78: 95–108.
- Sladek J, Sladek V, Krahulec S, et al. (2013) The MLPG analyses of large deflections of magneto-electro-elastic plates. *Engineering Analysis with Boundary Elements* 37(4): 673–682.
- Soh AK and Liu AJ (2005) On the constitutive equations of magneto-electro-elastic solids. *Journal of Intelligent Material Systems and Structures* 16(7–8): 597–602.
- Tan P and Tong L (2002) Modeling for the electro-magneto-thermo-elastic properties of piezoelectric-magnetic fiber reinforced composites. *Composites Part A: Applied Science and Manufacturing* 33(5): 631–645.
- Vaezi M, Shirbani MM and Hajnabey A (2016) Free vibration analysis of magneto-electro-elastic microbeams subjected to magneto-electric loads. *Physica E: Low-Dimensional Systems & Nanostructures* 75: 280–286.
- Vinyas M and Kattimani SC (2017a) Static studies of stepped functionally graded magneto-electro-elastic beam subjected to different thermal loads. *Composite Structures* 163: 216–237.
- Vinyas M and Kattimani SC (2017b) A finite element based assessment of static behavior of multiphase magneto-electro-elastic beam under different thermal loading. *Structural Engineering and Mechanics* 62(5): 519–535.
- Vinyas M and Kattimani SC (2017c) Static analysis of stepped functionally graded magneto-electro-elastic plates in thermal environment: a finite element study. *Composite Structures* 178: 63–86.
- Vinyas M and Kattimani SC (2017d) Hygrothermal analysis of magneto-electro-elastic plate using 3D finite element analysis. *Composite Structures* 180: 617–637.
- Wang J, Chen L and Fang S (2003) State vector approach to analysis of multilayered magneto-electro-elastic plates. *International Journal of Solids and Structures* 40(7): 1669–1680.
- Wang R, Han Q and Pan E (2011) Transient response of a bilayered multiferroic composite plate. *Acta Mechanica Sinica* 24(1): 83–91.
- Wei L, Kah SA and Ruilong H (2007) Vibration analysis of a ferromagnetic plate subjected to an inclined magnetic field. *International Journal of Mechanical Sciences* 49(4): 440–446.
- Xin L and Hu Z (2015a) Free vibration of layered magneto-electro-elastic beams by SS-DSC approach. *Composite Structures* 125: 96–103.
- Xin L and Hu Z (2015b) Free vibration of simply supported and multilayered magneto-electro-elastic plates. *Composite Structures* 121: 344–350.

Appendix I

The elemental stiffness matrices appearing in equation (19) are obtained as follows

$$\begin{aligned}
 [K_{tb}^e] &= \int_0^{a_e} \int_0^{b_e} [B_{tb}]^T [D_{tb}] [B_{tb}] dx dy, & [K_{trb}^e] &= \int_0^{a_e} \int_0^{b_e} [B_{tb}]^T [D_{trb}] [B_{rb}] dx dy \\
 [K_{rrb}^e] &= \int_0^{a_e} \int_0^{b_e} [B_{rb}]^T [D_{rrb}] [B_{rb}] dx dy, & [K_{t\phi}^e] &= \int_0^{a_e} \int_0^{b_e} [B_t]^T [D_{t\phi}] [B_\phi] dx dy \\
 [K_{t\psi}^e] &= \int_0^{a_e} \int_0^{b_e} [B_t]^T [D_{t\psi}] [B_\psi] dx dy, & [K_{t\theta}^e] &= \int_0^{a_e} \int_0^{b_e} [B_t]^T [D_{t\theta}] [N_\theta] dx dy \\
 [K_{r\phi}^e] &= \int_0^{a_e} \int_0^{b_e} [B_r]^T [D_{r\phi}] [B_\phi] dx dy, & [K_{r\psi}^e] &= \int_0^{a_e} \int_0^{b_e} [B_r]^T [D_{r\psi}] [B_\psi] dx dy \\
 [K_{r\theta}^e] &= \int_0^{a_e} \int_0^{b_e} [B_r]^T [D_{r\theta}] [N_\theta] dx dy, & [K_{\phi\phi}^e] &= \int_0^{a_e} \int_0^{b_e} [B_\phi]^T [D_{\phi\phi}] [B_\phi] dx dy \\
 [K_{\phi\psi}^e] &= \int_0^{a_e} \int_0^{b_e} [B_\phi]^T [D_{\phi\psi}] [B_\psi] dx dy, & [K_{\phi\theta}^e] &= \int_0^{a_e} \int_0^{b_e} [B_\phi]^T [D_{\phi\theta}] [N_\theta] dx dy \\
 [K_{\psi\psi}^e] &= \int_0^{a_e} \int_0^{b_e} [B_\psi]^T [D_{\psi\psi}] [B_\psi] dx dy, & [K_{\psi\theta}^e] &= \int_0^{a_e} \int_0^{b_e} [B_\psi]^T [D_{\psi\theta}] [N_\theta] dx dy
 \end{aligned} \tag{23}$$

$$\begin{aligned}
[K_{tt}^e] &= [K_{tb}^e] + [K_{ts}^e], [K_{trb}^e] = [K_{trs}^e] + [K_{tr}^e], [K_{rrb}^e] = [K_{rrs}^e] + [K_{rr}^e] \\
[K_{\theta\theta}^e] &= \int_0^{a_c} \int_0^{b_e} [N_\theta]^T [D_{\theta\theta}] [N_\theta] dx dy, \{F_{t\mathcal{L}m}\} = \int_0^{a_c} \int_0^{b_e} [N_t]^T [0 \ 0 \ P_z] dx dy \\
\{F_{r\mathcal{L}m}\} &= \int_0^{a_c} \int_0^{b_e} [N_r]^T [00M_z] dx dy, \{F_\phi\} = \int_0^{a_c} \int_0^{b_e} [N_\phi]^T [F_e] dx dy \\
\{F_\psi\} &= \int_0^{a_c} \int_0^{b_e} [N_\psi]^T [F_m] dx dy, \{F_{\bar{q}}\} = \int_0^{a_c} \int_0^{b_e} [N_\theta]^T \bar{q} dx dy c
\end{aligned} \tag{23}$$

where the rigidity matrices and vectors are given as follows

$$\begin{aligned}
[D_{tb}] &= \sum_{k=1}^N \int_{h_k}^{h_{k+1}} [C_b^k] dz, [D_{trb}] = \sum_{k=1}^N \int_{h_k}^{h_{k+1}} z [C_b^k] dz, [D_{t\theta}] = \sum_{k=1}^N \int_{h_k}^{h_{k+1}} [C_b^k] \{\alpha^k\} dz \\
[D_{t\phi}] &= \sum_{k=1}^N \int_{h_k}^{h_{k+1}} [e^k] dz, [D_{r\theta}] = \sum_{k=1}^N \int_{h_k}^{h_{k+1}} z [C_b^k] \{\alpha^k\} dz \\
[D_{trs}] &= \sum_{k=1}^N \int_{h_k}^{h_{k+1}} [C_s^k] dz, [D_{t\psi}] = \sum_{k=1}^N \int_{h_k}^{h_{k+1}} [q^k] dz \\
[D_{rrb}] &= \sum_{k=1}^N \int_{h_k}^{h_{k+1}} z^2 [C_b^k] dz, [D_{r\phi}] = \sum_{k=1}^N \int_{h_k}^{h_{k+1}} z [e^k] dz, [D_{r\psi}] = \sum_{k=1}^N \int_{h_k}^{h_{k+1}} z [q^k] dz \\
[D_{\phi\phi}] &= \sum_{k=1}^N \int_{h_k}^{h_{k+1}} [d^k] dz, [D_{\phi\psi}] = \sum_{k=1}^N \int_{h_k}^{h_{k+1}} [m^k] dz, [D_{\phi\theta}] = \sum_{k=1}^N \int_{h_k}^{h_{k+1}} [p_e^k] dz \\
[D_{\psi\psi}] &= \sum_{k=1}^N \int_{h_k}^{h_{k+1}} [\mu^k] dz, [D_{\psi\theta}] = \sum_{k=1}^N \int_{h_k}^{h_{k+1}} [p_m^k] dz, [D_{\theta\theta}] = \sum_{k=1}^N \int_{h_k}^{h_{k+1}} a dz
\end{aligned} \tag{24}$$

Appendix 2

The condensation technique used for solving equation (19) is as follows

$$\begin{aligned}
[K_1] &= [K_{t\psi}]^T - [K_{\psi\theta}] [K_{\theta\theta}]^{-1} [K_{t\theta}]^T, [K_2] = [K_{r\psi}]^T - [K_{\psi\theta}] [K_{\theta\theta}]^{-1} [K_{r\theta}]^T \\
[K_3] &= [K_{\phi\psi}]^T - [K_{\psi\theta}] [K_{\theta\theta}]^{-1} [K_{\phi\theta}]^T, [K_4] = [K_{\psi\psi}]^T - [K_{\psi\theta}] [K_{\theta\theta}]^{-1} [K_{\psi\theta}]^T \\
[K_5] &= [K_4]^{-1} [K_1], [K_6] = [K_4]^{-1} [K_2], [K_7] = [K_4]^{-1} [K_3] \\
[K_0] &= [K_4]^{-1} [K_{\psi\theta}] [K_{\theta\theta}], [K_8] = [K_{t\phi}]^T - [K_{\phi\theta}] [K_{\theta\theta}]^{-1} [K_{t\theta}]^T \\
[K_9] &= [K_{r\phi}]^T - [K_{\phi\theta}] [K_{\theta\theta}]^{-1} [K_{r\theta}]^T, [K_{10}] = [K_{\phi\phi}]^T - [K_{\phi\theta}] [K_{\theta\theta}]^{-1} [K_{\phi\theta}]^T \\
[K_{11}] &= [K_{\phi\psi}]^T - [K_{\phi\theta}] [K_{\theta\theta}]^{-1} [K_{\psi\theta}]^T, [K_{12}] = [K_8] - [K_{11}] [K_5] \\
[K_{13}] &= [K_9] - [K_{11}] [K_6], [K_{14}] = [K_{10}] + [K_{11}] [K_7], [K_{15}] = [K_{14}]^{-1} [K_{12}] \\
[K_{16}] &= [K_{14}]^{-1} [K_{13}], [K_{17}] = [K_{14}]^{-1} [K_{11}] [K_4]^{-1} \\
[K_{18}] &= [K_{14}]^{-1} [K_{\phi\theta}] [K_{\theta\theta}]^{-1} - [K_{14}]^{-1} [K_{11}] [K_0] \\
[K_{19}] &= [K_{tr}]^T + [K_{r\theta}] [K_{\theta\theta}]^{-1} [K_{t\theta}]^T
\end{aligned}$$

$$\begin{aligned}
[K_{20}] &= [K_{rr}]^T + [K_{r\theta}][K_{\theta\theta}]^{-1}[K_{r\theta}]^T, [K_{21}] = [K_{r\phi}]^T - [K_{r\theta}][K_{\theta\theta}]^{-1}[K_{\phi\theta}]^T \\
[K_{22}] &= [K_{r\psi}]^T - [K_{r\theta}][K_{\theta\theta}]^{-1}[K_{\psi\theta}]^T, [K_{23}] = [K_{19}] + [K_{22}][K_5] \\
[K_{24}] &= [K_{20}] + [K_{22}][K_6], [K_{25}] = [K_{21}] + [K_{22}][K_7] \\
[K_{26}] &= [K_{22}][K_4]^{-1}, [K_{27}] = [K_{r\theta}][K_{\theta\theta}]^{-1} - [K_{22}][K_0] \\
[K_{28}] &= [K_{23}] + [K_{25}][K_{15}], [K_{29}] = [K_{24}] + [K_{25}][K_{16}], [K_{30}] = -[K_{29}]^{-1}[K_{28}] \\
[K_{31}] &= [K_{29}]^{-1}([K_{26}] - [K_{25}][K_{17}]), [K_{32}] = [K_{29}]^{-1}[K_{25}][K_{14}]^{-1} \\
[K_{33}] &= [K_{29}]^{-1}([K_{27}] - [K_{25}][K_{18}]), [K_{34}] = [K_{tt}]^T + [K_{t\theta}][K_{\theta\theta}]^{-1}[K_{t\theta}]^T \\
[K_{35}] &= [K_{tr}]^T + [K_{t\theta}][K_{\theta\theta}]^{-1}[K_{r\theta}]^T, [K_{36}] = [K_{t\phi}]^T - [K_{t\theta}][K_{\theta\theta}]^{-1}[K_{\phi\theta}]^T \\
[K_{37}] &= [K_{t\psi}]^T - [K_{t\theta}][K_{\theta\theta}]^{-1}[K_{\psi\theta}]^T, [K_{38}] = [K_{34}] + [K_{37}][K_5], [K_{39}] = [K_{35}] + [K_{37}][K_6] \\
[K_{40}] &= [K_{36}] + [K_{37}][K_7], [K_{41}] = [K_{t\theta}][K_{\theta\theta}]^{-1} - [K_{37}][K_0], [K_{42}] = [K_{37}][K_4]^{-1} \\
[K_{43}] &= [K_{38}] + [K_{40}][K_{15}], [K_{44}] = [K_{39}] + [K_{40}][K_{16}], [K_{45}] = [K_{42}] - [K_{40}][K_{17}] \\
[K_{46}] &= [K_{41}] - [K_{40}][K_{18}], [K_{47}] = [K_{40}][K_{14}]^{-1}, [K_{48}] = [K_{43}] + [K_{44}][K_{30}] \\
[K_{49}] &= [K_{45}] - [K_{44}][K_{31}], [K_{50}] = [K_{46}] - [K_{44}][K_{33}] \\
[K_{51}] &= [K_{47}] - [K_{44}][K_{32}], [K_{52}] = -[K_{44}][K_{29}]^{-1} \\
[K_{eq}] &= [K_{48}], \{F_{eq}\} = [K_{49}]\{F_{\psi}\} + [K_{50}]\{F_{\theta}\} + [K_{51}]\{F_{\phi}\} - [K_{52}]\{F_{r,m}\} + \{F_{t,m}\}
\end{aligned} \tag{25}$$

The effect of ϕ can be deduced as follows

$$\begin{aligned}
[K_{tt}^e]\{d_t^e\} + [K_{tr}^e]\{d_r^e\} + [K_{t\phi}^e]\{\phi^e\} &= 0 \\
[K_{tr}^e]^T\{d_t^e\} + [K_{rr}^e]\{d_r^e\} + [K_{r\phi}^e]\{\phi^e\} &= 0 \\
[K_{t\phi}^e]^T\{d_t^e\} + [K_{r\phi}^e]^T\{d_r^e\} - [K_{\phi\phi}^e]\{\phi^e\} &= 0 \\
\{\phi^e\} &= [K_{\phi\phi}^e]^{-1}[K_{t\phi}^e]\{d_t^e\} + [K_{\phi\phi}^e]^{-1}[K_{r\phi}^e]\{d_r^e\} \\
[K_{tr}^e]\{d_t^e\} + [K_{rr}^e]\{d_r^e\} + [K_{r\phi}^e][K_{\phi\phi}^e]^{-1}[K_{t\phi}^e]\{d_t^e\} + [K_{r\phi}^e][K_{\phi\phi}^e]^{-1}[K_{r\phi}^e]\{d_r^e\} \\
\{d_t^e\} &= [K_{tr}^e] + [K_{r\phi}^e][K_{\phi\phi}^e]^{-1}[K_{t\phi}^e] + \{d_r^e\} [K_{rr}^e] + [K_{r\phi}^e][K_{\phi\phi}^e]^{-1}[K_{r\phi}^e] \\
[K_{\phi\phi,1}^e]\{d_t^e\} + [K_{\phi\phi,2}^e]\{d_r^e\} &= 0 \\
\{d_r^e\} &= -[K_{\phi\phi,2}^e]^{-1}[K_{\phi\phi,1}^e]\{d_t^e\} \\
[K_{tt}^e]\{d_t^e\} + [K_{tr}^e]\{d_r^e\} + [K_{t\phi}^e][K_{\phi\phi}^e]^{-1}[K_{t\phi}^e]\{d_t^e\} + [K_{t\phi}^e][K_{\phi\phi}^e]^{-1}[K_{r\phi}^e]\{d_r^e\} &= 0 \\
\{d_t^e\} &= [K_{tt}^e] + [K_{t\phi}^e][K_{\phi\phi}^e]^{-1}[K_{t\phi}^e] + \{d_r^e\} [K_{tr}^e] + [K_{t\phi}^e][K_{\phi\phi}^e]^{-1}[K_{r\phi}^e] \\
[K_{\phi\phi,3}^e]\{d_t^e\} + [K_{\phi\phi,4}^e]\{d_r^e\} &= 0 \\
[K_{\phi\phi,3}^e]\{d_t^e\} - [K_{\phi\phi,4}^e][K_{\phi\phi,2}^e]^{-1}[K_{\phi\phi,1}^e]\{d_t^e\} &= 0 \\
[K_{\phi\phi,eq}^e] &= [K_{\phi\phi,3}^e] - [K_{\phi\phi,4}^e][K_{\phi\phi,2}^e]^{-1}[K_{\phi\phi,1}^e] \\
[K_{\phi\phi,1}^e] &= [K_{tr}^e] + [K_{r\phi}^e][K_{\phi\phi}^e]^{-1}[K_{t\phi}^e] \\
[K_{\phi\phi,2}^e] &= [K_{rr}^e] + [K_{r\phi}^e][K_{\phi\phi}^e]^{-1}[K_{r\phi}^e]
\end{aligned}$$

$$\begin{aligned}
[K_{\phi\phi_3}] &= [K_{tt}^e] + [K_{t\phi}^e] [K_{\phi\phi}]^{-1} [K_{t\phi}^e] \\
[K_{\phi\phi_4}] &= [K_{tr}^e] + [K_{t\phi}^e] [K_{\phi\phi}]^{-1} [K_{r\phi}^e]
\end{aligned} \tag{26}$$

The effect of ψ can be deduced as follows

$$\begin{aligned}
[K_{tt}^e] \{d_t^e\} + [K_{tr}^e] \{d_r^e\} + [K_{t\psi}^e] \{\psi^e\} &= 0 \\
[K_{tr}^e]^T \{d_t^e\} + [K_{rr}^e] \{d_r^e\} + [K_{r\psi}^e] \{\psi^e\} &= 0 \\
[K_{t\psi}^e]^T \{d_t^e\} + [K_{r\psi}^e]^T \{d_r^e\} - [K_{\psi\psi}^e] \{\psi^e\} &= 0 \\
[K_{eq_ \psi\psi}] &= [K_{\psi\psi_3}] - [K_{\psi\psi_4}] [K_{\psi\psi_2}]^{-1} [K_{\psi\psi_1}] \\
[K_{\psi\psi_1}] &= [K_{tr}^e] + [K_{r\psi}^e] [K_{\psi\psi}]^{-1} [K_{t\psi}^e] \\
[K_{\psi\psi_2}] &= [K_{rr}^e] + [K_{r\psi}^e] [K_{\psi\psi}]^{-1} [K_{r\psi}^e] \\
[K_{\psi\psi_3}] &= [K_{tt}^e] + [K_{t\psi}^e] [K_{\psi\psi}]^{-1} [K_{t\psi}^e] \\
[K_{\psi\psi_4}] &= [K_{tr}^e] + [K_{t\psi}^e] [K_{\psi\psi}]^{-1} [K_{r\psi}^e] \\
\{\psi^e\} &= [K_{\psi\psi}]^{-1} [K_{t\psi}^e] \{d_t^e\} + [K_{\psi\psi}]^{-1} [K_{r\psi}^e] \{d_r^e\} \\
\{d_r^e\} &= - [K_{\psi\psi_2}]^{-1} [K_{\psi\psi_1}] \{\psi^e\}
\end{aligned} \tag{27}$$

The effect of θ can be deduced as follows

$$\begin{aligned}
[K_{tt}^e] \{d_t^e\} + [K_{tr}^e] \{d_r^e\} + [K_{t\theta}^e] \{\theta^e\} &= 0 \\
[K_{tr}^e]^T \{d_t^e\} + [K_{rr}^e] \{d_r^e\} + [K_{r\theta}^e] \{\theta^e\} &= 0 \\
[K_{t\theta}^e]^T \{d_t^e\} + [K_{r\theta}^e]^T \{d_r^e\} - [K_{\theta\theta}^e] \{\theta^e\} &= 0 \\
[K_{eq_ \theta\theta}] &= [K_{\theta\theta_3}] - [K_{\theta\theta_4}] [K_{\theta\theta_2}]^{-1} [K_{\theta\theta_1}] \\
[K_{\theta\theta_1}] &= [K_{tr}^e] + [K_{r\theta}^e] [K_{\theta\theta}]^{-1} [K_{t\theta}^e] \\
[K_{\theta\theta_2}] &= [K_{rr}^e] + [K_{r\theta}^e] [K_{\theta\theta}]^{-1} [K_{r\theta}^e] \\
[K_{\theta\theta_3}] &= [K_{tt}^e] + [K_{t\theta}^e] [K_{\theta\theta}]^{-1} [K_{t\theta}^e] \\
[K_{\theta\theta_4}] &= [K_{tr}^e] + [K_{t\theta}^e] [K_{\theta\theta}]^{-1} [K_{r\theta}^e] \\
\{\theta^e\} &= [K_{\theta\theta}]^{-1} [K_{t\theta}^e] \{d_t^e\} + [K_{\theta\theta}]^{-1} [K_{r\theta}^e] \{d_r^e\} \\
\{d_r^e\} &= - [K_{\theta\theta_2}]^{-1} [K_{\theta\theta_1}] \{\theta^e\}
\end{aligned} \tag{28}$$